Black TiO_2 nanotube arrays decorated with Ag nanoparticles for enhanced visible-light photocatalytic oxidation of salicylic acid

Milivoj Plodinec[1,3], *Ivana Grčić*[2], *Marc G. Willinger*[3,4], *Adnan Hammud*[3], *Xing Huang*[3], *Ivana Panžić*[1], *Andreja Gajović*[1*]

[1] Ruđer Bošković Institute, Bijenička 54, HR-10000 Zagreb, Croatia
[2] University of Zagreb, Faculty of Geotechnical Engineering, Hallerova aleja 7, HR-42000 Varaždin
[3] Fritz-Haber-Institute der Max-Planck-Gesellschaft, Faradayweg 4-6, D-14195 Berlin, Germany
[4] Department of Colloid Chemistry, Max Planck Institute of Colloids and Interfaces, Am Mühlenberg 1, 14476 Potsdam, Germany

ABSTRACT: Novel forms of black TiO_2 nanotubes-based photocatalysts for water purification were prepared. Two features were combined: decoration of TiO_2 nanotube arrays with Ag nanoparticles (sample TiO_2-NT's@Ag) and further hydrogenation of this material (TiO_2-NT's@Ag-HA). Obtained photocatalysts show high efficiency for degradation of salicylic acid, a typical water-borne pollutant. The photocatalysts considerably exceed the photocatalytic properties of TiO_2 nanotubes and commercial TiO_2 P25 taken as a reference for modelling of the photocatalytic process. The comparison of photocatalytic activities between novel photocatalyst was based on a numerical approach supported by the complex kinetic model. This model allowed a separate study of different contributions on overall degradation rate. The contributions include: salicylic acid photolysis, photocatalysis in UVB, UVA and in the visible part of applied simulated solar irradiation. The superior photocatalytic performance of the photocatalyst TiO_2-NT's@Ag-HA, particularly under visible irradiation, was explained by the combined effect of a local surface plasmon resonance (LSPR) due to Ag nanoparticles and creation of additional energy levels in band-gap of TiO_2 due to Ti^{3+} states at nanotube surfaces. The presence of Ag also positively influence charge separation of created electron-holes pairs. The synergy of several effects was quantified by a complex

* Corresponding author e-mail address: gajovic@irb.hr

kinetic model through the factor of synergy, f_{Syn}. Stability testing indicated that the catalysts were stable for at least 20 hours. The novel design of catalysts, attached on Ti foils, presents a solid base for the development of more efficient photocatalytic reactors for large-scale with a long-term activity.

KEYWORDS: black TiO_2 nanotubes arrays, Ag decoration, salicylic acid photodegradation, solar irradiation, kinetic model

1. INTRODUCTION

The TiO_2 based materials are one of the most studied materials in the last 40 years, with the applications in various fields such as: solar cells [1], photocatalysis [2], water splitting [3], batteries [4], for bone and dental implants due to biocompatibility [5], gas sensing due to change in electrical and optical properties [6]. On the other hand, TiO_2 nanotubes are widely investigated from its beginnings in 2001, when Grimes and co-workers for the first time synthesized TiO_2 nanotube arrays by electrochemical oxidation of Ti-foil [7]. It is a relatively simple process and it is possible to apply the same procedure on the large scale to grow uniform array of TiO_2 nanotubes. Advantages of obtained TiO_2 nanotubes are temperature and chemical stability, relatively low cost of production, film flexibility, and high specific surface area [8]. The anodization process enables to precisely control the morphological parameters of thin film growth: film thickness, nanotubes diameter, wall thickness, surface roughness [8]. Those parameters can be controlled by variation of: applied DC voltage, type of electrolyte, the concentration of water and fluoride ions, reaction time [8]. The anodization parameters also influence the adhesion of the TiO_2 nanotube arrays to Ti substrate, so the adhesion can be enhanced by two-step anodization process described by Yu et al. [9]. Advantages of TiO_2 nanotube arrays compared to other TiO_2 morphologies are a high specific area (many reaction centers at the nanotube surface), good carrier mobility due to the wire like morphology, and environmental stability [10]. The photocatalytic activity of pure TiO_2 nanotubes is limited due to the relatively large band gap of 3.2 eV for anatase and 3.02 eV for rutile (bulk materials) [11]. In order to increase activity, it is essentially to modify the surface; to dope or to decorate the nanotubes with the aim to tune band gap in the desired range of solar irradiation absorption (visible and near infrared, NIR) [12].

In the last 30 years there were many different approaches and attempts to increase photo catalytic activity of TiO_2 by doping with non-metal and metal atoms [13-23], depositing or decorating the surface of TiO_2 nanostructure (nanoparticles, nanowire, nanotubes, nanobelts) by noble metal nanoparticles (Pt, Pd, Au, Ag) or metal oxide nanoparticles (WO_3, Cu_2O, CeO_2, Fe_2O_3) [23-33]. The electron trapping in the junction between noble metal nanoparticles and TiO_2 is determined by the work function of the metal, which is usually larger than in TiO_2. The electron-hole pair can be formed by photon absorption at the surface of TiO_2, formed electron would be transferred from conduction band (CB) of TiO_2 to metal nanoparticles. Schottky barrier, which is formed at the junction, leads to efficient charge separation due to the existence of an internal electric field between TiO_2 and metal nanoparticles and acts as a trap for the generated charge carriers.

The photocatalytic materials decorated by noble metals are classified as plasmonic photocatalyst [34]. The noble metal nanoparticles can be uniformly deposited (Au, Ag, Pd, Pt) by one of the chemical methods with the particles size in the range of a few nanometers up to several 100 nm. The aim of deposit nanoparticles at the surface of the nanotubes is to increase UV and visible light absorption, to ensure better charge carrier separation, an increase of local electric field and localized surface plasmon resonance (LSPR). By the variation of the nanoparticles size, it is possible to tune the wavelength of absorption maximum [34]. The embedding of the noble metal nanoparticles at the surface of the semiconductor provide several beneficial effects. In the plasmonic photocatalysis, there are two distinct features which contribute to better performances of the plasmonic photocatalysts in comparison to conventional ones. Those are: (i) Schottky junction and (ii) localized surface plasmon resonance (LSPR). There is forced electron-hole separation close to the interface and fast lane charge transfer due to the first feature. While LSPR induced several more effects: visible light response, enhanced UV-vis absorption, reduced electron-hole diffusion

length, enhanced local electric field, LSPR electron-hole generation, local heating effects and molecule polarization effect [34]. Yu et al. [35] prepared a new metal–semiconductor nanocomposite plasmonic photocatalyst by depositing AgCl nanoparticles into the self-organized TiO_2 nanotubes, followed by partial reduction of Ag^+ ions in the surface region of AgCl particles. Such photocatalyst showed a high visible-light photocatalytic activity for the photocatalytic degradation of methyl orange. Different authors studied the influence of the particle size of noble-metal elements (Ag, Au) that decorate the TiO_2 nanostructures on the intensity and red shift of the absorbance in visible region [36, 37].

The ‘’black’’ TiO_2 nanostructures obtained by annealing in the reductive atmospheres (H_2, Ar/H_2, CO, NO) has drawn a lot of attention recently. Reduced TiO_2 nanostructures have better properties for applications in DSSC cells, water splitting and photocatalysis compared to non-reduced TiO_2 [38, 39]. One of the reasons is narrowed band gap (< 3 eV), which allows the photocatalytic activity of TiO_2 in the visible range of solar irradiation. The narrower band gap could result in a higher efficiency in the photocatalytic reactions [40]. Recent studies gave an explanation in terms of creation of Ti^{3+} states during thermal treatment of TiO_2 nanotubes in the reductive atmosphere [41, 42]. High-temperature annealing in the inert oxygen-free atmosphere, in a vacuum or reductive atmosphere lead to the release of O_2 molecules and formation of Ti^{3+} ions, usually at the nanotubes surfaces. Reduced nanotubes showed absorption in the visible part of solar spectra and better conductivity. These effects can be explained through the appearance of the high density of localized donor states which are created in forbidden gap of TiO_2 due to the formation of Ti^{3+}, which actually represents electron donor state closely to the bottom of the conduction band of TiO_2. The high-pressure H_2 treatment of TiO_2 nanotubes lead to anatase-like “black titania”, showing a high open-circuit photocatalytic hydrogen production rate without the presence of a co-catalyst. Through these processes, it is possible to create the most of 1% Ti^{3+}

from Ti^{4+}, before crystal structure collapsed. This process is reversible till some point, because exposure to air or O_2 atmosphere leads to oxidation. Similar as Ti^{3+}, the oxygen vacancies also increase absorption in the visible part of solar spectra. Chen and co-workers firstly reported on the synthesis of "black" TiO_2 nanoparticles by annealing in the reductive atmosphere (H_2 atmosphere at 200 □C for 5 days and pressure 20 Bar) [38]. The nanoparticles had a core-shell structure with crystalline TiO_2 inner part of nanoparticles and outer amorphous shell. Naldoni et al. synthesized TiO_2 nanocomposites with core-shell structure, with crystalline core and amorphous 2 nm thick shell [43]. They explained narrowing of the bandgap by the existence of defects such as Ti^{3+} and oxygen vacancies which create energy states inside the bandgap. These states allowed the absorption and intraband transition in the energy region smaller than 3.2 eV. Tao et al. applied a different approach to obtain narrowed bandgap of 2.1 eV. They obtained TiO_2 phase forms on the surface of rutile TiO_2 (011) by oxidation of bulk titanium interstitials [44], which resulted in the similar photocatalytic activity due to TiO_2 self-doping with Ti^{3+} during annealing process in a reductive atmosphere of CO or NO [45]. Wang et al. proposed that H-doped amorphous shell plays the same role as Ag or Pt loading on TiO_2 nanocrystals, which induces the localized surface plasmon resonance and black coloration, resulting in enhanced photocatalytic activity [46]. Wu et al. [47] applied the electrochemical hydrogenation doping for the introduction of interstitial hydrogen ions and oxygen vacancies. Similar process was used by Zhao et al. [48] to reduce Ti^{4+} to Ti^{3+}, that is approved by XPS measurements. In our previous work [49], powder of titanate ($H_2Ti_3O_7$) nanotubes decorated by Ag was studied for photocatalytic properties. We have shown that annealing of the protonated type of titanate nanotubes in Ar/H_2 induce a transition to TiO_2 anatase phase nanoparticles can be used as efficient powder catalyst. Moreover, $H_2Ti_3O_7$ nanotubes decorated with Ag nanoparticles

after annealing in the reductive atmosphere (Ar/H_2) had two times higher photocatalytic activity than those which were annealed in Ar/H_2 but not decorated with Ag

With the aim to prepare the efficient easy-handling photocatalyst for purification of waste water from the industry, we studied the modification and decoration of titanium oxide nanotube arrays (TiO_2-NT's) that are completely attached on titanium foil. In that manner, there are no nanoparticles left in purified water as in the case of the use of suspended powder catalyst (e.g. P25 TiO_2). To increase the efficiency of the TiO_2-NT's photocatalyst caused by LSPR, titanium oxide nanotubes arrays were decorated by Ag nanoparticles (sample TiO_2-NT's@Ag) and subsequently reduced by annealing in hydrogen (TiO2-NT's@Ag-HA) with the aim to narrow band gap of titania. The photocatalysts were evaluated by photodegradation of salicylic acid (SA) in aqueous solution. SA was chosen as a model pollutant due to its widespread use in dyestuff, resins and aspirin production, which results in its release to the environment through various waste streams. SA was listed as a pollutant in precipitation, surface waters (approx. 0.1 $\mu g\ L^{-1}$) and as a constituent of humic material in drinking waters. It may be released to the aquatic environment in wastewater discharges from industry and even sewage treatment facilities [50].

The TiO_2-NT's arrays were modified by Ag using similar procedures as in our previous research [49]. In this work it was shown that TiO_2 nanotubes formed by anodization process on Ti foil decorated with Ag nanoparticles after annealing in the reductive atmosphere (TiO_2@Ag-HA) have the best overall photocatalytic performance, even 1.53 times larger than commercial P25. The increase in the efficiency is explained by the combined effect of localized surface plasmon resonance (LSPR) of the silver nanoparticles and the increased absorption of visible light and NIR due to the reduction of TiO_2 in hydrogen and formation of defects such as Ti^{3+} and oxygen vacancies. These defects create energy states inside the

bandgap that allow an interband transition in the energy region smaller than 3.2 eV that can be achieved by visible light.

The kinetic study presented in this work resulted in a complex kinetic model which allowed a separate study of the photochemical degradation of salicylic acid and photon absorption effects in UVB, UVA and visible part of applied simulated solar irradiation. These discrete photon absorption study supported detailed analysis and quantification of fundamental photocatalytic phenomena. Moreover, the absorption in UVB and UVA part of applied irradiation was described with relative coefficients with TiO_2 P25 as a reference. Contribution from the absorption terms was accounted in the overall degradation rate equations, along with the factor of synergy, f_{Syn}. Introduction of f_{Syn}. in the model, resulted in quantification of the influence of underlying phenomena on the activity, other than pure absorption of incoming irradiation, e.g., surface defects as Ti^{3+} and LSPR.

2. MATERIALS AND METHODS

2.1 Materials

The following materials were used: titanium foil (10x10 cm, purity 99.5 %, Sigma Aldrich), Ethanol (Fluka, 98%), deionized water, $AgNO_3$(Kemika, purity 99.8%), gas mixture Ar/H_2 (95% Argon,5% hydrogen, Messer, purity 5.0). Salicylic acid (SA) p.a. the grade was obtained as a free-of-charge sample from Pliva, Croatia and used without further purification. A model solution of 0.2 mmol L^{-1} of SA was prepared (pH 4). The degradation of SA in the samples was evaluated in terms of SA concentration decrease and mineralization degree. The concentration of SA was determined using HPLC, Shimadzu, with SUPELCO C18 column, length 250 mm, internal diameter 4.6 mm and UV (diode array) detection

(DAD) at 303 nm. The analyses were carried out by binary flow elution with mobile phase solvents A and B at a flow rate of 0.6 and 0.4 mL min^{-1}, respectively. Solvent A consisted of 0.5:99.5 (v/v) methanol: 0.1 M phosphoric acid and solvent B was 100% methanol. This method allows simultaneous determination of SA and its degradation by-products: 2,5-dihydroxybenzoic acid (gentinsic acid), 2,3-dihydroxybenzoic acid, 3,4,5-trihydroxybenzoic acid (gallic acid), hydroquinone, catechol and resorcinol using multi-wavelength DAD. The sum of their concentration expressed through the C atom balance was used to evaluate the conversion of aromatics to lumped short-chain carboxylic acids. The mineralization degree was determined by measuring the total organic content of model wastewater by Total Organic Carbon analyzer, TOC-V_{CPN}, Shimadzu, Japan.

2.2 Synthesis

The TiO_2 nanotube arrays were obtained by anodizing a titanium metal foil (purity 99.7%, size 1.5x1.5 cm and thickness 0.25 mm). The anodization was carried out at room temperature in a conventional two-electrode cell using a direct current (DC) power supply A Pt foil was used as the counter electrode and a Ti-foil served as the anode. The electrolyte was ethylene glycol containing 0.3 wt.% NH_4F and 2 vol.% distilled water. The self-organized and well-aligned TiO_2 nanotube arrays were fabricated at 60 V for 3 h. As a result of the anodization process, the TiO_2 nanotubes were etched of in the titanium foil. The details of chemical reactions and phenomena acting during formation of a nanotubes by anodization are described in our previous work [51]. Following anodization, the specimens were rinsed in deionized water and ethanol, and dried in a cool air stream. The anodized specimens were, then, thermally treated in a tube furnace at 500 □C (heating/cooling rate of 2 □C/min) for 2 h. The anodization parameters stated above were found by optimization of the anodization

process to obtain samples with TiO_2 layers that were attached to the Ti surface strong enough to resist all the future treatment.

The photo-reduction process was used for decoration of TiO_2 nanotubes with Ag nanoparticles, similar to one explained in our previous work [46]. Precisely, the Ti-foils with thin film TiO_2 nanotubes arrays (TiO_2 NT's) were immersed in 0.05 M solution of $AgNO_3$; the solution was continuously stirred under UV light for 3h at 80 □C. After the decoration of TiO_2 nanotubes with Ag nanoparticles (TiO_2 NT's@Ag), the foil was rinsed with ethanol and deionized water and dried for 1 h at 80□C in air. TiO_2 NT's and TiO_2 NT's@Ag samples were annealed in a reductive atmosphere (Ar/H_2) for 3h at 500 □C, temperature rate was 5 °C/min. Obtained samples were assigned as TiO_2 NT's-HA and TiO_2 NT's@Ag-HA.

2.3 Characterization

The Raman spectroscopy (RS) measurements were performed using Horiba, Jobin–Yvon T64000 spectrometer with argon-ion laser Coherent, Innova 400 operating at 514.5 nm for the excitation. The Raman spectra were collected in micro- Raman mode with a multi-channel CCD detector. A laser power of 20 mW at the sample and an objective with a 50 magnification were used.

The morphology, surface and chemical composition of modified samples were studied by the scanning electron microscopy (SEM) using a Hitachi S-4800 with a cold FEG (Field Emission Gun). The images were taken in secondary electron (SE) mode with an acceleration voltage of 15 kV. The energy dispersive spectroscopy (EDS) analysis was also done at 15 kV.

For the transmission electron microscopy (TEM) analysis modified samples were prepared in the cross-section by Gatan precision ion polishing system (PIPS) and ion beam etching system. The TEM, high-resolution TEM (HRTEM) and high angle annular dark field

scanning transmission electron microscopy (HAADF STEM) imaging were performed on the TEM Philips CM200F and FEI TITAN 80-300 kV.

For the EELS data acquisition, double Cs aberration corrected (TEM and STEM) JEOL-ARM 200CF equipped with GIF Quantum Energy Filters spectrometer for the high resolution and DualEELS spectra acquisition was used. Measurements were performed under following conditions: dispersion 0.1 eV/channel and integration time for each pixel on EELS maps of 2 seconds. The pixel size was 1.5 nm. Afterwards, the collected spectra were corrected for dark current and channel-to-channel gain variation. The samples of EELS measurements were prepared in lamela's form by the FEI-Helios Dual-beam system.

The UV–vis-NiR diffuse-reflectance spectroscopy was utilized for the optical reflectance characterization and band-gap calculation of the pure and Ag-decorated synthesized TiO_2 nanotubes before and after annealing in the hydrogen atmosphere. The optical absorption spectra were measured with a UV–vis-NiR Perkin–Elmer Lambda 650 high-performance spectrophotometer a wavelength range from 300 nm to 900 nm, with a step size 1nm. The samples were mounted by the scotch tape at the sample holder and analyzed in reflective mode with the aperture 0.5 x 1.0 cm.

2.4 Photocatalytic activity

Photocatalytic experiments were performed in a flow cell (4.5 cm in diameter, 2 cm in height) working in total recirculation using a peristaltic pump (V_{total} = 40 mL, flow rate Q = 67 mL min^{-1}). Plates with the photocatalytic film were put on the cell bottom, whereby directly irradiated [52], so the catalysts were positioned perpendicular to the light irradiation. Prior to experiments, SA solutions ($C_{0,\,SA}$ = 0.5, 0.2, 0.1 mmol dm^{-3}) were recirculated in the dark over the plates to achieve the sorption equilibrium. The sources of irradiation were: (i) full-spectrum compact fluorescent bulb simulating solar spectra with high UVB; high colour

rendering Ra98/Class 1A with colour temperature of 6500K (Exo Terra, 20W), and (ii) incandescent bulb emitting only visible light (Osram Daylight, 100W). The UVB and UVA intensities were measured by UVP UVX radiometer, fitted with the corresponding UVB and UVA sensors. For the incandescent bulb, both UVA and UVB intensities were measured as 0.0 mW cm^{-2}, indicating a complete absence of UV radiation in the spectrum of this bulb. For the full-spectrum bulb, given intensities on the cell top (at free water surface) were: $I_{UVB,0}$ = 2.92 mW cm^{-2} and $I_{UVA,0}$= 3.43 mW cm^{-2}. Intensities at film surface which were accounted for the incident photon flux at photocatalysts surface were: $I_{UVB,f}$ = 0.18 mW cm^{-2} and $I_{UVA,f}$ = 2.65 mW cm^{-2}. Note that is much lower than $I_{UVB,0}$, due to the absorption of light by SA. The $I_{UVB,f}$ was obtained from radiometric readings from the bottom of the cell filled with the SA solution. Experiments were performed in triplicates to discard possible experimental error and to check the reusability of the photocatalysts. With the aim to study the stability of the catalysts additional ten consecutive cycles of photocatalytic experiments were done using full-spectrum compact fluorescent bulb simulating solar spectra.

3. NUMERICAL APPROACH FOR QUANTIFICATION OF PHOTOCATALYTIC ACTIVITY

The novelty presented in this work is the quantification of the photocatalytic activity of prepared materials, compared to a reference, TiO_2 P25. The latter was used as a reference since it is the most common commercial photocatalysts with an appropriate activity. The the main hypothesis in this study was the achievement of advantageous photocatalytic properties of TiO_2 NT's@Ag and TiO_2 NT's@Ag-HA compared to anatase film. Tentatively, the photocatalytic properties of these films would also exceed the properties of the efficient

commercial TiO_2, i.e., TiO_2 P25 in the case when the same was prepared in the form of thin film. Having in mind the specific form of novel photocatalyst and inability to produce the film having only pure TiO_2 P25 with similar morphological characteristics, the comparative quantification was done using the numerical method according to the algorithm presented as follows.

The detailed kinetic model was developed to include the contribution from direct photolysis as well as the contribution from UVB, UVA and visible light to photocatalytic degradation of SA.

The total rate of SA degradation ($r_{SA,T}$, kmol m^{-3} s^{-1}) can be described as follows:

$$r_{SA,T} = r_p + \underbrace{r_{ph}^{UVB} + r_{ph}^{UVA} + r_{ph}^{vis}}_{r_{ph}\text{ - photocatalysis}} \quad (1)$$

In Eq. (1), r_p is the rate of direct photolysis of SA under UVB irradiation, r_{ph} is the rate of photocatalytic degradation where superscripts *UVB*, *UVA* and *vis* denominate contributing term. Note that pseudo-monochromatic irradiation (310 and 365 nm) was assumed for UVB and UVA part of irradiation in further calculations. This simplification can be found in literature as well [53].

To define the rate of photolysis, near-surface light absorption by SA was assumed. First-order photolysis rate constant k_p (s^{-1}) was given, Eq. (2) [54];

$$k_p(\lambda) = 2.3\Phi_{SA}(\lambda)\varepsilon_{SA}(\lambda)W(\lambda)\frac{A}{V}l \quad (2)$$

where Φ_{SA} is the photochemical quantum yield for SA photolysis, ε_{SA} is the molar extinction coefficient (L mol^{-1} cm^{-1}), W is the incident light intensity (Einstein cm^{-2} s^{-1}), A, V and l are the surface of the reaction cell, total volume and solution depth, respectively. The λ stands for the wavelength of concern, which in this case is exactly 310 nm, taking into account the assumed monochromatic irradiation over UVB region. The photochemical quantum yield can

be calculated using the observed rate of SA photolysis. The latter will be reported in the *Results and Discussion* section.

$$\Phi_{\mathrm{SA,\,310nm}} = \frac{k_{\mathrm{p,\,obs}}}{2.3\varepsilon_{\mathrm{SA,\,310\,nm}} W_{\mathrm{UVB}} (A/V) l} \tag{3}$$

The molar extinction coefficient was obtained from spectrophotometric analysis of SA solutions of different concentration (data not shown). The $\varepsilon_{\mathrm{SA,\,310\,nm}}$ was found to be 2710 L $\mathrm{mol^{-1}}$ $\mathrm{cm^{-1}}$. The incident light intensity was obtained from Eq. (4).

$$W_{\mathrm{UVB}} = \frac{I_{\mathrm{UVB,0}}}{N_{\mathrm{A}} \frac{hc}{\lambda}} \tag{4}$$

The $I_{\mathrm{UVB,\,0}}$ ($\mathrm{Wm^{-2}}$) is the irradiation intensity at the free water surface determined by radiometric measurements, N_{A}, h and c represents Avogadro's number, Planck constant and speed of light, respectively. Resultant incident light intensity at 310 nm was 7.562×10^{-5} Einstein $\mathrm{cm^{-2}}$ $\mathrm{s^{-1}}$.

Finally, quantum yield was $\Phi_{\mathrm{SA,\,310\,nm}} = 8.59 \times 10^{-8}$. Note that calculation was made per unit of the reaction cell, meaning that reported quantum yield can be used for calculation of photolytic rates in other reactor configurations.

The rate of photocatalytic reaction can be written as follows:

$$r_{\mathrm{ph}} = -k_{\mathrm{SA,\,int}} \left[\left(\mu_{310\mathrm{nm}} I_{\mathrm{UVB,\,f}} \right)^{m_1} + \left(\mu_{365\mathrm{nm}} I_{\mathrm{UVA,\,f}} \right)^{m_2} + \left(P_{\mathrm{ph}}^{vis} \right)^{m_3} \right] C_{\mathrm{SA}} \tag{5}$$

In Eq. (5). $k_{\mathrm{SA,\,int}}$ ($\mathrm{m\ s^{-1}\ W^{-0.5}}$) represent the intrinsic reaction rate constant for SA degradation over irradiated photocatalytic films. Contributing terms: $\mu_{310\mathrm{nm}} I_{\mathrm{UVB,f}}$, $\mu_{365\mathrm{nm}} I_{\mathrm{UVA,f}}$ and $P_{\mathrm{ph}}^{\mathrm{vis}}$ represent the rate of photon absorption in UVB, UVA and visible part of simulated solar spectra, respectively, which are proportional to the rate of reaction [55,56]. The exponents m_1, m_2 and m_3 represent the order of the reaction with respect to the rate of photon absorption

in related part of solar spectra. The half-order dependence in well-irradiated system was assumed ($m = m_1 = m_2 = m_3 = 0.5$).

To estimate the relative precedence of studied films compared to the reference, the rate equation was modified to Eq. (6). It needs to be noted that well-mixed, lump reaction system with a uniform distribution of incident irradiation on the film surface was considered.

$$r_{ph} = -k_{SA,\,int}\left(\mu'_{app,310nm}\,\mu_{P25,310nm} I_{UVB,\,f} + \mu'_{app,365nm}\,\mu_{P25,365nm} I_{UVA,\,f} + P_{ph}^{vis}\right)^{m} C_{SA} \quad (6)$$

Herein, $\mu'_{app,310nm}$ and $\mu'_{app,365nm}$ are the apparent relative absorption coefficient of the film ($=\mu_{film}/\ \mu_{P25}$). Those numbers simply suggest how many times the studied film absorb more irradiation than the referent TiO_2 P25. The $\mu_{P25,\,310\,nm}$ and $\mu_{P25,\,365\,nm}$ are referent absorption coefficients calculated from the specific absorption coefficient for TiO_2 and its mass per square meter of the film ($= \kappa^* m_{cat}/A_f$). The specific absorption coefficients (κ^*) for TiO_2 P25 can be found in the literature [57-59]. Used values are summarized in Table 1. Mass of the photocatalytic film per area of the film was estimated at 5.66×10^{-5} kg m^{-2}. Finally, the term P_{ph}^{vis} (in W m^{-2}) represent the overall rate of photon absorption in the visible part of simulated solar spectra. This term was determined experimentally from the experiments where only the visible light was used, Eq. (7).

$$P_{ph}^{vis} = \left(\frac{k^{vis}_{SA,obs}}{k_{SA,\,int}}\right)^{2} \quad (7)$$

Note that $k^{vis}_{SA,\,obs}$ are observed pseudo-first order reaction rate constants for photocatalytic degradation of SA over TiO_2 NT's, TiO_2 NT's@Ag and TiO_2 NT's@Ag-HA under visible light (presented in the following section), while the intrinsic reaction rate constant was reported in our previous work [57], where it was expressed as 4×10^{-7} min^{-1} W$^{-0.5}$ m$^{1.5}$. In this study, the surface rates are used and the $k_{SA,\,int}$ was recalculated to 1.4×10^{-8} s^{-1} W$^{-0.5}$ m.

Resultant photon absorption in the visible part of the spectra, P_{ph}^{vis}, values are shown in Table 1. The presented modelling approach is however incomplete. By expressing the total photocatalytic rates with Eq. (6), one can assume that only the absorption of light in a visible part of solar spectra and the enhanced absorption in UVB and UVA were responsible for the enhancement of the overall SA degradation rates. The absurd values of $\mu'_{app,310nm}$ and $\mu'_{app,365nm}$, approaching several thousands and millions (Table 1), suggest the incorrect assumptions. Having in mind previously mentioned the influence of the combined effect of local surface plasmon resonance of Ag and creation of amorphous layer with Ti^{3+} and oxygen vacancies states at nanotubes surfaces, the rate can be written as follows; introducing the overall factor of synergy (f_{Syn}) into equation (Eq. (8)).

$$r_{ph} = -\left[k_{SA,\,int} \left(\mu''_{app,310nm}\, \mu_{P25,310nm} I_{UVB,\,f} + \mu''_{app,365nm}\, \mu_{P25,365nm} I_{UVA,\,f} + P_{ph}^{vis} \right)^{m} \right] f_{Syn} C_{SA} \quad (8)$$

Hereby, $\mu''_{app,310nm}$ and $\mu''_{app,365nm}$ are the apparent relative absorption coefficient of the film ($=\mu_{film}/\ \mu_{P25}$). For simplification purpose, the apparent relative absorption coefficient for TiO_2 NT's was assumed to be 1. This assumption was justified by the similarities in the optical properties between TiO_2 NT's and TiO_2 P25 in the range from 300 – 400 nm (Fig. 7). Namely, for both photocatalysts, absorption is almost uniform in UVB part, while reduces approaching longer wavelengths in UVA part of spectrum (data from Figure 7. compared to reported data [60-62]). The average values of absorbances in the UV-vis absorbance spectra of TiO_2 NT's@Ag and TiO_2 NT's@Ag-HA compared to the average values for TiO_2 NT's were used to determine $\mu''_{app,310nm}$ and $\mu''_{app,365nm}$. All calculated values are reported in Table 1.

4. RESULTS AND DISCUSSION

4.1 Structural and optical characterization of TiO_2 NT's samples

Raman spectroscopy was applied as a method of choice to study the influence of the decoration with Ag and hydrogenation on the structure of the obtained TiO_2 nanotubes array. Raman spectra of TiO_2 NT's, TiO_2 NT's@Ag and TiO_2 NT's@Ag-HA were shown in Figure 1. The spectra of all the samples contained the observed bands assigned to five bands characteristics for anatase crystalline phase (144, 199, 396, 514 and 636 cm^{-1}) [63]. In the case of TiO_2 NT's@Ag-HA sample, the additional band at 246 cm^{-1} (black arrow, Figure 1) was observed due to annealing in a reductive atmosphere. The appearance of this band can be explained by the existence of structural defects at the surface of nanotubes as results of annealing in the reductive atmosphere [40, 64].

The scanning electron microscopy was applied to study the morphology of the samples and influence of the modification and the decoration with Ag,. The SEM images show that TiO_2 NT's obtained by simple anodization process have the inner diameter in the range of 55-60 nm and an outer diameter in the range of 70-75 nm (Figure 2). It can also be observed that Ag nanoparticles were uniformly deposited on the TiO_2 nanotubes and the size distribution are broad, which is preferable to improve efficiency due to the LSPR effect. Larger particles (size up to 100 nm) were seen at the surface of TiO_2 NT's, while smaller are distributed both at the surface and inside the tubes as was additionally confirmed by TEM techniques (as will be shown later). It could be noticed that the surface of TiO_2 NT's@Ag-HA appeared cleaner than the surface of TiO_2 NT's@Ag due to annealing in the reducing gas atmosphere (Ar/H_2) during which the adsorbed hydrocarbons and other impurities at the surface were removed.

The HAADF-STEM images of cross-section performed on the TiO_2 NT's@Ag sample, shown in the Figure 3 a) and 3 b), indicate that TiO_2 nanotubes have a length around 2100 nm

and wall thickness between 14 and 20 nm. The specimens were anodized for 3 h and grew to less than 3 μm in Fig. 3a. However, by using different electrolyte, nanotubes can grow to more than 5 μm within 30 min of anodization [65, 66].

It was shown that Ag nanoparticles are uniformly distributed through the whole length of nanotubes (Figure 3 a) and b)) in the average size of 5.7 nm for the Ag nanoparticles inside the tubes (Figure 3 f)). The HRTEM analysis showed that nanotubes are in the anatase crystal phase (Figure 3 c) and 3 d)) which is in agreement with Raman results (Figure 1). It could also be observed in Figure 3 e) that Ag nanoparticles during photo deposition were embedded into nanotube surface.

The TiO_2 nanotube arrays were activated by the high-temperature annealing in the reductive atmosphere, which results with partial amorphization and surface disorder of the nanotubes surfaces (Figure 4) similar as in a case described in previous work [67]. The amorphous layer on the TiO_2 nanoparticles surface obtained by treatment of titanate nanotubes (in form of powder) in hydrogen were also observed in our previous work [46] and in previous studies with thermal treatment of titania nanostructures in the reduced atmosphere [38-49]. Here, it can be observed typical core-shell structure (crystalline core and thin amorphous shell) of TiO_2 nanotube from nanotubes array of sample TiO_2 NT's@Ag-HA. It is expected that this layer would contain defects as oxygen vacancies and Ti^{3+} states.

In order to confirm the presence of Ti^{3+} in nanotubes amorphous shell after reduction, we performed EELS spectroscopy measurements on nanotubes separated from the array by FIB. The analysis of energy-loss near-edge fine structure (ELNES) of Ti-$L_{2,3}$ edge and O k-edge were carried out. As is known from the literature that Ti L-edge in case of anatase and rutile core-loss EELS spectra consists of four major peaks (two doublets, t_{2g} and e_g) which represent L_3 and L_2 edge, and splitted p orbitals, $2p_{3/2}$ and $2p_{1/2}$ states. It can be observed on

the Figure 5 in ELNES of the Ti-$L_{2,3}$ edge and the O-k edge of the TiO_2 NT's-HA and TiO_2 NT's@Ag-HA.

The spectra of both samples were recorder over the whole thickness of nanotube wall, and at the surface of the nanotube. Comparing the spectra of the nanotube in core region and surface, the EELS spectra of a Ti-$L_{2,3}$ edge obtained at nanotube surface of both samples is slightly shifted to lower energy loss values (Figure 5a and 5c) which imply the existence of Ti^{3+} electronic states on the nanotubes surface. Also, the EELS spectra obtained at nanotubes surface looks similar to the spectra of amorphous TiO_2 what is in agreement with previous observations of order-disorder core-shell structure in the literature after high-temperature treatment in the reductive atmosphere [67, 68]. On the Figure 5b and 5d are shown the EELS spectra of O k-edge. It could be observed that there is almost no difference between spectra at the core of nanotubes wall and surface.

The EELS spectra of pristine TiO_2 NT's and nanotubes treated in a reductive atmosphere, TiO_2 NT's-HA and TiO_2 NT's@Ag-HA, were compared in Figure 6. The spectra of TiO_2 NT's sample can be assigned to EELS spectra of the anatase phase. For the reduced samples similar behaviour was observed (Figure 5). The splitting of Ti L_2 and L_3-edge was less pronounced in reduced samples. Additionally, spectra are slightly shifted to lower energy loss due to creation of Ti^{3+} states.

As reported recently [69], Pd nanoparticles can catalyse the reduction of TiO_2 rutile in H_2 at room temperature through the generation of highly active hydrogen species which interact with TiO_2 lattice and creates Ti^{3+}, oxygen vacancies and even influencing the surface disorder. Without the Pd, several days are necessary for the hydrogenation of the TiO_2, under high pressure (20.0 bar) or temperature up to 700 °C. Surprisingly, the treatment of TiO_2 matrix decorated with Ag nanoparticles did not improve the reduction. However, we observed a successful reduction of TiO_2 nanotube array with and without decoration with Ag,

already after the samples were annealed for 3h at 500 □C using even less reductive atmosphere (Ar/H_2). Our observation of successful TiO_2 hydrogenation can be explained by nanotubular form of samples (which guarantee large surface of the material), but also by anatase form of TiO_2 nanotubes.

With the aim to study the influence of the decoration with Ag and hydrogenation on broadening of the spectral region of the light absorption and narrowing of the TiO_2 nanotubes band gap, UV-vis measurements were performed. The results of UV-vis spectroscopy of the TiO_2 NT's arrays show that in case of TiO_2 NT's-HA and TiO_2 NT's@Ag-HA, the absorbance is shifted to the visible and NiR region of spectra (Figure 7a and 7b). The bandgap of all studied samples was shown by the dashed line in the Figure 7c. As could be observed the samples TiO_2 NT's and TiO_2 NT's-HA have similar main bandgap around 3.1 eV, but sample TiO_2 NT's-HA have additional transition around 1.6 eV. In the case of samples TiO_2 NT's@Ag and TiO_2 NT's@Ag-HA there are following band gap 2.7 and 2.3 eV, respectively. The deposition of small Ag nanoparticles at the surface of nanotubes significantly increase the absorption in the visible region of spectra. As it was already mentioned in the introduction, in the case of plasmonic photocatalyst there is a strong increase of absorption in the visible part of the spectra and partially in the UV region. The same behaviour of absorption enhancement we observed in our measurements (Figure 7). Annealing of TiO_2 nanotubes decorated with Ag nanoparticles in the reductive atmosphere Ar/H_2 additionally influenced the structure and optical properties of materials. The annealing in the reductive atmosphere created additional states in the gap between the conductive and valence band of TiO_2, as is schematically shown in Figure 8, thus improving the absorption in the visible region. During reduction process the structural defects are created, such as Ti^{3+}, as was proven by EELS measurements. Those defects influenced the electronic structure of TiO_2 nanotubes, which resulted in a macroscopic effect as narrowing of the bandgap. The

created defects could be the traps for the recombination of created electron-holes pairs, but due to the silver nanoparticles, this effect is suppressed.

In Figure 8, the schematic view of the influence of the silver on the optical and electrical properties of TiO_2 nanotubes are shown. On the Ag - TiO_2 interface there is a creation of Schottky barrier, which suppresses the recombination of light-induced charge carriers (e-h) due to the internal local electric field at the Ag/TiO_2 NTs interfaces. On the other hand, the Ag nanoparticles induced LSPR effect which contributed to the final concentration of free electron in the conduction band of TiO_2 which can participate in the photocatalytic reaction. The LSPR is size dependent effect so different sizes of the Ag nanoparticles obtained in our work absorbed different Vis and NIR wavelengths. Therefore, if the LSPR electrons have enough energy to overcome the Schottky barrier at the interface, the electrons would directly transport into the conduction band of TiO_2. W. Hou and S. B. Cronin [70] in the review paper state that for the better combined effect of TiO_2 and noble metal nanoparticles (Ag, Au) and higher photocatalytic efficiency there is a requirement for doping of TiO_2 to create lower energy states inside the bandgap of TiO_2. They said that crucial factor to achieve a maximum of plasmon enhancement is that spectral enhancement of the metal nanoparticles overlap with the spectral absorption of the semiconductor photocatalyst and with the spectrum of the illumination source. They also said that most of the electron which is created due to LSPR effect don't have enough high energy to overcome the Schottky barrier due to low Fermi level in the noble metal nanoparticles. Noble metal nanoparticles (Ag) due to the LSPR effect creates intense local electric fields and previous simulation in the literature shown that electric field intensity of local plasmonic ‘’hot spots’’ can reach as 1000 times that of the incident electromagnetic field [71, 72]. Which means that the ‘’hot spots’’ region can have electron-hole pairs generation 1000 higher than in the case of an incident electromagnetic field. Thus, enhancement in the amount of photo-induced charge generation is happening

locally in the TiO_2. This enhancement will be possible only if there are additional lower energy states are created inside the bandgap of TiO_2 [70-73]. In our case additional energy states are formed due to the defects such as: Ti^{3+} and oxygen vacancies in the TiO_2 which enables the light absorption below the bandgap of TiO_2 Due to previously mentioned reasons, which were proved theoretically and experimentally, one can conclude that combined effect of noble metal nanoparticles at the surface of TiO_2 NT's and defects state inside of bandgap TiO_2 NT created by subsequently annealing in the reduced atmosphere leads to highest phocatalytic performances as will be shown and highest absorption as it was already shown in the Figure 7.

4.2 Photocatalytic properties of TiO_2 NT's samples

Results for the photocatalytic oxidation of salicylic acid using full-spectrum solar simulation irradiation source and only visible light are given in Fig. 9. The photocatalytic activity is observed in the following range: TiO_2 NT's@Ag-HA > TiO_2 NT's@Ag > TiO_2 NT' in both cases. The significantly higher photocatalytic activity of TiNT@Ag-HA under visible irradiation compared to the other studied catalysts can be ascribed to its significant absorption in the visible regions of solar irradiation due to the effects explained previously. Some authors show that the nonmetal doping of TiO_2 with elements such as nitrogen and fluorine are responsible for the nanotubes' photoactivity under visible light [74, 75], but EELS measurements (not shown) of our samples indicated that neither nitrogen nor fluorine were inbuilt during the nonotubes' fabrication process. Given experimental data points are the mean results of three series of experiments. The photocatalytic activities of studied photocatalysts did not vary during repeated experiments suggesting the reusability and photocatalytic stability of as-prepared samples.

Kinetics of photocatalytic degradation of salicylic acid under simulated solar irradiation and visible light, are shown in Fig. 9a and 9b, respectively. Under simulated solar irradiation, photochemical degradation of salicylic acid was observed (Fig. 9a), which was expected since SA contains chromophores that absorb at wavelengths 290-315 nm making it susceptible to direct photolysis [76]. The photocatalytic degradation of SA is much faster when TiO_2 NT's@Ag and TiO_2 NT's@Ag-HA were used as photocatalysts, disregarding the source of irradiation (Fig. 9). TiO_2 NT's@Ag-HA film seems to be an efficient photocatalyst even only under visible irradiation.

Regarding SA degradation intermediates and overall mineralization estimated based on TOC measurements, results are given in Figure 10a. Results were compared using the C atom balance. The theoretical value of TOC ascribed to the aromatic compounds *i* detected by HPLC were calculated from Eq. (9), using a number of C atoms in aromatic compounds N_i(C), molar masses (M_i) and mass concentration ($c_{i,m}$) for each compound.

$$\mathrm{TOC}_{\mathrm{aromatics}} = \sum_i \frac{12.01 N_i(\mathrm{C})}{M_i} c_{i,m} \tag{9}$$

The conversion of aromatic intermediates was higher than the achieved mineralization extent. Expected aliphatic intermediates, i.e. short-chain carboxylic acids cannot be readily degraded towards CO_2 which accounts for higher residual TOC values. The mineralization efficiency was highest when TiO_2 NT's@Ag-HA film was applied, for both irradiation sources. Mineralization under visible light is negligible, however the percentage of residual aromatics is lower after 120 min of photocatalytic reaction, pointing at the slow ongoing conversion of aromatics towards aliphatic compounds.

In the preliminary analysis, kinetics of SA photocatalytic degradation was evaluated according to the pseudo-first order reaction rate model in batch reaction system (Eq. (10)):

$$\frac{dc_{\mathrm{SA}}}{dt} = -k_{\mathrm{SA,\,obs}}\, c_{\mathrm{SA}} \tag{10}$$

where c_{SA} is a concentration of salicylic acid, while $k_{SA,\,obs}$ is the pseudo-first order rate constant in min^{-1}, and it was evaluated through the linear regression of $\ln(c_{SA}/c_{SA,0})$ vs. time (Eq. (11)).

$$\ln\frac{c_{SA}}{c_{SA,0}} = -k_{SA,\,obs}\,t \tag{11}$$

Corresponding values of $k_{SA,\,obs}$, degradation half-time, $t_{1/2}$ and determination coefficient R^2 are given in Table 2. Based on experimental results, adsorption of SA on films was insignificant. The pseudo-first order rate constant for the direct photolysis under simulated solar irradiation of aqueous salicylic acid was found to be $\approx 2.0 \times 10^{-3}$ min^{-1}. The obtained value corresponds well with the reported value of $< 3 \times 10^{-4}$ min^{-1} (0.02 hr^{-1}) [68] having in mind that the peak intensity of applied irradiation in UVB region (310 nm) is almost 10 times higher than the average intensity of UVB irradiation accounted for natural sunlight .

Repeated experiments were done in a row to test the stability of prepared photocatalytic films: TiO_2 NT's, TiO_2 NT's@Ag, TiO_2 NT's@Ag-HA under simulated solar irradiation. The resulting $k_{SA,\,obs}$ of sets of 10 experiments (cycles) are shown in Fig. 10b . The uniformity of the pseudo-first order rate constant for SA degradation ($k_{SA,\,obs}$, min^{-1}) is observed when using TiO_2 NT's, TiO_2 NT's@Ag, TiO_2 NT's@Ag-HA as photocatalysts, leading to a conclusion that prepared films are equally active and thus stable for at least 20 hours.

The preliminary kinetics study based on pseudo-first order reaction rate constant was insufficient to describe underlying phenomena. The detailed kinetic model was developed to include the contribution from direct photolysis as well as the contribution from UVB, UVA and visible light to photocatalytic degradation of SA (see section 3.; Eq. (1)).

The main hypothesis in this study was the achievement of advantageous photocatalytic properties of TiO_2 NT's@Ag and TiO_2 NT's@Ag-HA compared to anatase film. Tentatively, the photocatalytic properties of these films would exceed the properties of the efficient commercial TiO_2, i.e. TiO_2 P25 in the case when the same would be prepared in a form of

thin film, hypothetically, as described in Section 3. Calculated values of model parameters are reported in Table 1. Comparison of kinetic models and experimental results are shown in Fig. 11. A simple model (Eq. (10)) is in accordance with the developed complex model (Eqs. (1), (2) and (8)).

The novelty within this work is the overall factor of synergy (f_{Syn}). This factor summarized the influences of the combined effect of local surface plasmon resonance of Ag and creation of amorphous layer with Ti^{3+} and oxygen vacancies states at nanotubes surfaces (responsible for the decrease of E_g and absorption in the visible part of the spectrum). The f_{Syn} includes all underlying phenomena which resulted in higher rates of radical species generation on active sites, such as OH•, O_2•$^-$ etc. The f_{Syn} were given for all studied photocatalytic films (Table 1). The value of 1.13 was obtained for TiO_2 NT's@Ag, while it was 2.56 for TiO_2 NT's@Ag-HA. Such difference suggests that the film obtained by annealing in reductive atmosphere indeed poses additional states in the gap between the conductive and valence band which is also confirmed by determined P_{ph}^{vis}, and the structural defects are created, such as Ti^{3+} and oxygen vacancies, which influence on the electronic structure of TiO_2 nanotubes and account for overall synergy. Using the presented kinetic modeling approach (Eq. (8)) meaningful values of apparent relative absorption coefficients are presented (μ"). Enhanced light absorption throughout the solar spectra can be concluded form the following: (i) the $\mu"_{app,310nm}$ and $\mu"_{app,365nm}$ calculated for TiO_2 NT's@Ag and TiO_2 NT's@Ag-HA are higher than those assumed for anatase film and TiO_2 P25, (ii) the P_{ph}^{vis} values significantly increased in the following order: TiO_2 NT's < TiO_2 NT's@Ag < TiO_2 NT's@Ag-HA. The results from kinetic modeling supported by presented experimental results confirmed the conclusions made entirely based on the structural and optical characterization of the film samples.

5. CONCLUSIONS

The influence of high-temperature annealing of TiO_2 nanotube arrays decorated with silver nanoparticles in the reductive Ar/H_2 atmosphere on the photocatalytic activity was studied. Three different samples of TiO_2 nanotubes were prepared and studied: pure TiO_2 nanotube arrays, TiO_2 nanotubes array where interior and exterior of all the nanotubes are decorated by silver nanoparticles (TiO_2 NT's@Ag), and TiO_2 NT's@Ag treated at 500 °C in a hydrogen atmosphere (TiO_2 NT's@Ag-HA). The synthesis of nanotubes by anodization of Ti foils is simple, fast and inexpensive as well as further deposition of Ag and treatment in hydrogen.

The absorbance of solar irradiation was extended into the visible region for the samples TiO_2 NT's@Ag and TiO_2 NT's@Ag-HA. Surface plasmon resonance of deposited Ag nanoparticles was responsible for the increase of absorption in the case of TiO_2 NT's@Ag. In sample TiO_2 NT's@Ag-HA, in addition to surface plasmon resonance, the defects created by hydrogen treatment generate additional transition state inside the bandgap of TiO_2 and further increase absorbance.

The efficiency of photocatalysis was tested on salicylic acid, recognized as a typical environmental pollutant. The obtained results show much better photocatalytic performance of TiO_2 NT's@Ag than commercial TiO_2 P25, while the best performance was observed for TiO_2 NT's@Ag-HA.

The detailed kinetic study showed the contribution from photon absorption effects in UVB, UVA and visible part of the simulated solar spectrum. Results showed the enhanced absorption of irradiation through the spectrum, in comparison with P25. The P_{ph}^{vis} values indicate the well-enhanced absorption rates in the following range TiO_2 NT's < TiO_2 NT's@Ag < TiO_2 NT's@Ag-HA. The results from kinetic modeling supported the understanding of the influence of a visible part of the solar spectrum to overall photocatalytic

performances. The photocatalytic effect is enlarged by the synergy of absorbance in UV part (in bulk of TiO_2 NTs) and visible part of solar irradiation (explained by combined effects of surface plasmon resonance of Ag and creation of amorphous layer with Ti^{3+} on the surface of TiO_2 NTs). The determined factors of synergy (f_{Syn}) for TiO_2 NT's@Ag and TiO_2 NT's@Ag-HA were 1.36 and 2.71, respectively.

The additional substantial advantage of studied photo-catalysts compared to the TiO_2 nanoparticles based materials (as P25) is easy handling. They are formed and completely attached on titanium plates that can be easily removed from the solution after the photocatalytic reaction. Since the rate of photocatalytic degradation of model pollutant is quite high when solar simulation was applied (less than 2 h is needed for its half-degradation if TiO_2 NT's@Ag-HA film was used), this gives a certain merit to a possible use of this type of photocatalysts on a larger scale. Obtained results are promising in the way of designing efficient reactors for the future application in the field of waste-water purification using TiO_2 membranes or by constructing reactor walls made of TiO_2 nanotubes array decorated by Ag nanoparticles and reduced in the Ar/H_2 atmosphere.

ACKNOWLEDGMENT

Funding: This work has been supported in part by Croatian Science Foundation under the project IP-2014-09-9419, a Croatian-Germany bilateral project financed by DAAD agency and Ministry of science and education of Croatia and Centre of Excellence for Advanced Materials and Sensing Devices, Ruđer Bošković Institute, Zagreb, Croatia.

REFERENCES:

[1] B.O'Regan, and M. Grätzel, A Low-cost, High-Efficiency Solar Cell Based on Dye-Sensitized Colloidal TiO_2 Films, Nature 353 (1991) 737-740.

[2] M. A. Fox, and M. T. Dulay, Heterogeneous Photocatalysis, Chem. Rev. 93 (1993) 341-357.

[3] A. Fujishima, K. Honda, Electrochemical Photolysis of Water at a Semiconductor Electrode, Nature 238 (1972) 37-38.

[4] W. Guo, X. Xue, S. Wang, C. Lin, Z. L. Wang, An Integrated Power Pack of Dye-Sensitized Solar Cell and Li Battery Based on Double-Sided TiO_2 Nanotube Arrays, Nano Lett. 12 (2012) 2520-2523.

[5] R. Van Noort, Titanium: The Implant Material of Today, J. Mat. Sci. 22 (1987) 3801-3811.

[6] X. X. Zhang, J.B. Zhang, Y.C. Jia, P.Xiao, J. Tang, A Pt-Doped TiO_2 Nanotube Arrays Sensor for Detecting SF_6 Decomposition Products, Sensors 12 (2012) 3302–3313.

[7] D. Gong, C. A. Grimes, O. K. Varghese, W. Hu, R. S. Singh, Z. Chen, and E. C. Dickey, Titanium Oxide Nanotube Arrays Prepared by Anodic Oxidation, J. Mater. Res. 16 (2001) 3331-3334.

[8] K. Lee, A. Mazare, P. Schmuki, One-Dimensional Titanium Dioxide Nanomaterials: Nanotubes, Chem. Rev. 114 (19) (2014) 9385–9454.

[9] D. Yu, X. Zhu, X. Zhen, X. Zhong, Q. Gui, S. Ye, S. Zhang, X. Chen, D. Li, Facile method to enhance the adhesion of TiO2 nanotube arrays to Ti substrate, ACS Applied Materials & Interfaces 6 (2014) 8001-8005.

[10] F. Fabregat-Santiago, E. M. Barea, J. Bisquert, G. K. Mor, K. Shankar, C. A. Grimes, High Carrier Density and Capacitance in TiO_2 Nanotube Arrays Induced by Electrochemical Doping, J. Am. Chem. Soc. 130 (2008) 11312–11316.

[11] J.-G. Li, T. Ishigaki, and X. Sun, Anatase, Brookite, and Rutile Nanocrystals via Redox Reactions under Mild Hydrothermal Conditions: Phase-Selective Synthesis and Physicochemical Properties, J. Phys. Chem. C 111 (2007) 4969-4976.

[12] I. Paramasivam, H. Jha, N. Liu, P. Schmuki, A review of photocatalysis using self-organized TiO_2 nanotubes and other ordered oxide nanostructures, Small 8 (2012) 3073-3103.

[13] R. Beranek, M. J. Macak, M. Gartner, K. Meyer, P. Schmuki, Enhanced visible light photocurrent generation at surface-modified TiO_2 nanotubes, Electrochim. Acta 54 (2009) 2640-2646.

[14] M. Anpo, Photocatalysis on titanium oxide catalysts: Approaches in achieving highly efficient reactions and realizing the use of visible light, Catal. Surv. Jpn. 1 (1997) 169-179.

[15] K. Yang, Y. Dai, B. J. Huang, Understanding Photocatalytic Activity of S- and P-Doped TiO_2 under Visible Light from First-Principles, Phys. Chem. C 111 (2007) 18985-18994.

[16] K. Yang, Y. Dai, B. Huang, Origin of the Photoactivity in Boron-Doped Anatase and Rutile TiO_2 Calculated from First Principles, Phys. Rev. B 76 (2007) 195201-195206.

[17] T. Umebayashi, T. Yamaki, H. Itoh, K. J. Asai, Analysis of Electronic Structures of 3d Transition Metal-Doped TiO_2 Based on Band Calculations, Phys. Chem. Solids 63 (2002) 1909-1920.

[18] J. Osorio-Guillen, S. Lany, A. Zunger, Atomic-Control of Conductivity vs. Ferromagnetism in Wide-Gap Oxides via Selective Doping: V, Nb, and Ta in Anatase TiO_2, Phys. Rev. Lett. 100 (2008) 036601-036604.

[19] Y. Wang, D. Doren, Electronic structures of V-doped Anatase TiO_2, Solid State Commun. 136 (2005) 142-146.

[20] C. D. Valentin, G. Pacchioni, H. Onishi, A. Kudo, Cr/Sb. co-Doped TiO_2 from First Principles Calculations, Chem. Phys. Lett. 469 (2009) 166-171.

[21] G. Shao, Red Shift in Manganese- and Iron-Doped TiO_2: A DFT +U Analysis, J. Phys. Chem. C 113 (2009) 6800-6808.

[22] A. Czoska, S. Livraghi, M. Chiesa, E. Giamello, S. Agnoli, S. Granozzi, E. Finazzi, C. D. Valentin, G. Pacchioni, The Nature of Defects in Fluorine-Doped TiO_2, J. Phys. Chem. C 112 (2008) 8951-8956.

[23] M. Fernandez-Garcia, A. Martinez-Arias, A. Fuerte, J. C. Conesa, Nanostructured Ti−W Mixed-Metal Oxides: Structural and Electronic Properties, J. Phys. Chem. B 109 (2005) 6075-6083.

[24] I. Paramasivam, J. M. Macak, A. Ghicov, P. Schmuki, Enhanced Photochromism of Ag Loaded Self-Organized TiO_2 Nanotube Layers, Chem. Phys. Lett. 445 (2007) 233-237.

[25] I. Paramasivam, J. M. Macak, P. Schmuki, Photocatalytic Activity of TiO_2 Nanotube Layers Loaded with Ag and Au Nanoparticles, Electrochem. Commun. 10 (2008) 71-75.

[26] J. M. Macak, P. J. Barczuk, H. Tsuchiya, H. M. Z. Nowakowska, A. Ghicov, M. Chojak, S. Bauer, S. Virtanen, P. J. Kulesza, P. Schmuki, Self-organized Nanotubular TiO_2 Matrix as Support for Dispersed Pt/Ru Nanoparticles: Enhancement of the electrocatalytic oxidation of methanol, Electrochem. Commun. 7 (2005) 1417-1422.

[27] S. K. Mohapatra, N. Kondamudi, S. Banerjee, M. Misra, Functionalization of Self-Organized TiO_2 Nanotubes with Pd Nanoparticles for Photocatalytic Decomposition of Dyes Under Solar Light Illumination, Langmuir 24 (2008) 11276-11281.

[28] P. Aurora, P. Rhee, L. Thompson, Titania Nanotube Supported Gold Photoanodes for Photoelectrochemical Cells, J. Electrochem. Soc. 157 (2010) 152-155.

[29] H. Yu, X. Wang, H. Sun, M. J. Huo, Photocatalytic Degradation of Malathion in Aqueous Solution Using an Au-Pd-TiO_2 Nanotube Film, Hazard. Mater. 184 (2010) 753-758.

[30] B. Lu, X. Li, T. Wang, E. Xieb, Z. Xu, WO_3 nanoparticles decorated on both sidewalls of highly porous TiO_2 nanotubes to improve UV and visible-light photocatalysis, J. Mater. Chem. A 1 (2013) 3900–3906.

[31] J. Zhang, Y. Wang, C. Yu, X. Shu, L. Jiang, J. Cui, Z. Chen, T. Xiee Y. Wu, Enhanced Visible-Light Photoelectrochemical Behaviour of Heterojunction Composite with Cu_2O Nanoparticles-Decorated TiO_2 Nanotube Arrays, New J. Chem. 38 (2014) 4975-4984.

[32] Y. Yu, X. J. Yu, S. Yang, Preparation and Characterization of CeO_2 Decorated TiO_2 Nanotube Arrays Photoelectrode and its Enhanced Photoelectrocatalytic Efficiency for Degradation of Methyl Orange, J. Mat. Sci.: Materials in Electronics 26 (2015) 5715-5723.

[33] A. I. Kontos, V. Likodimos, T. Stergiopoulos, D. S. Tsoukleris, P. Falaras, I. Rabias, G. Papavassiliou, D. Kim, J. Kunze, P. Schmuki, Self-Organized Anodic TiO_2 Nanotube Arrays Functionalized by Iron Oxide Nanoparticles, Chem. Mater. 21 (2009) 662-672.

[34] X. Zhang, Y. L. Chen, R. S. Liu, D. P. Tsai, Plasmonic photocatalysis, Rep. Prog. Phys. 76 (2013) 046401-046444.

[35] J. Yu, G. Dai, B. Huang, Fabrication and Characterization of Visible-Light-Driven Plasmonic Photocatalyst Ag/AgCl/TiO_2 Nanotube Arrays, J. Phys. Chem. C 113 (2009) 16394–16401.

[36] K. Chen, X. Feng, R. Hu, Y. Li, K. Xie, Y. Li, H. Gu, Effect of Ag Nanoparticle Size on the Photoelectrochemical Properties of Ag Decorated TiO_2 Nanotube Arrays, J. Alloys Comp. 554 (2013) 72-79.

[37] Z. Xu, J. Yu, G. Liu, Enhancement of Ethanol Electrooxidation on Plasmonic Au/TiO_2 Nanotube Arrays, Electrochem. Commun. 13 (2011) 1260-1263.

[38] X. Chen, L. Liu, Y.P. Yu, S.S. Mao, Increasing Solar Absorption for Photocatalysis with Black Hydrogenated Titanium Dioxide Nanocrystals, Science 331 (2011) 746-750.

[39] G. Wang, H. Wamg, Y. Ling, Y. Tang, X. Yang, C.R. Fitzmorris, C. Wang, J.Z. Zhang, Y. Li, Hydrogen-Treated TiO_2 Nanowire Arrays for Photoelectrochemical Water Splitting, Nano Lett. 11 (2011) 3026-3033.

[40] W.Q. Han, Y. Zhang, Phases $Ti_nO_{2n-1}TinO_{2n-1}$ Nanowires: Formation, Optical, and Transport Properties, Appl. Phys. Lett. 92 (2008) 203117-3.

[41] Y. C. Nah, I. Paramasivam, P. Schmuki, Doped TiO_2 and TiO_2 Nanotubes: Synthesis and Applications, ChemPhysChem 11 (2010) 2698-2713.

[42] N. Liu, C. Schneider, D. Freitag, M. Hartmann, U. Venkatesan, J. Müller, E. Spiecker, P. Schmuki, Black TiO_2 Nanotubes: Cocatalyst-Free Open-Circuit Hydrogen Generation, Nano Lett. 14 (2014) 3309-3313.

[43] A. Naldoni, M. Allieta, S. Santangelo, M. Marelli, F. Fabbri, S. Capelli, C.L. Bianchi, R. Psaro, V.D. Santo, Effect of Nature and Location of Defects on Bandgap Narrowing in Black TiO_2 Nanoparticles, J. Am. Chem. Soc. 134 (2012), 7600-7603. and references within.

[44] J. Tao, T. Luttrell, M. Batzill, A Two-Dimensional Phase of TiO_2 with a Reduced Bandgap, Nat. Chem. 3 (2011) 296.

[45] F. Zuo, L. Wang, T. Wu, Z. Zhang, D. Borchardt, P. Feng, Self-Doped Ti^{3+} Enhanced Photocatalyst for Hydrogen Production under Visible Light, J. Am. Chem. Soc. 132 (2010) 11856-11857.

[46] Z. Wang, C. Yang, T. Lin, H. Yin, P. Chen, D. Wan, F. Xu, F. Huang, J. Lin, X. Xie, M. Jiang, H-Doped Black Titania with Very High Solar Absorption and Excellent Photocatalysis Enhanced by Localized Surface Plasmon Resonance, Adv. Funct. Mater. 23 (2013) 5444-5450.

[47] H. Wu, D. Li, X. Zhu, C. Yang, D. Liu, X. Chen, Y. Song, L. Lu, High-performance and renewable supercapacitors based on TiO2 nanotube array electrodes treated by an electrochemical doping approach, Electrochimica Acta 116 (2014) 129-136.

[48] S. Zhao, Y. Chen, Z. Zhao, L. Jiang, C. Zhang, J. Kong, X. Zhu, Enhanced capacitance of TiO2 nanotubes topped with nanograss by H3PO4 soaking and hydrogenation doping, Electrochimica Acta 266 (2018) 233-241

[49] M. Plodinec, A. Gajović, G. Jakša, K. Žagar, M. Čeh, High-Temperature Hydrogenation of Pure and Silver-Decorated Titanate Nanotubes to Increase their Solar Absorbance for Photocatalytic Applications, J. Alloy. Compd. 591 (2014) 147-155.

[50] HSDB, The Hazardous Substances Data Bank, In: TOXNET, Toxicology Data Network (2014) http://toxnet.nlm.nih.gov/cgi-bin/sis/htmlgen? HSDB Last accessed: May 9 2014

[51] V. Mandić, M. Plodinec, I. Kereković, K. Juraić, V. Janicki, D. Gracin, A. Gajović, A. Moguš-Milanković, and M- G. Willinger, Tailoring anatase nanotubes for the photovoltaic device by the anodization process on behalf of microstructural features of titanium thin film, Solar energy materials and solar cells 168 (2017) 136-145.

[52] I. Grčić, I. Brnardić, D. Mutavdžić Pavlović, V. Mandić, S. Papić, Photocatalytic Activity of Synthesized Titanate Nanotubes and Nanoribbons vs. Commercial TiO_2 under Artificial Solar and Visible Irradiation using 17ß-Estradiol as Model Micropollutant, Desalin. Water Treat. 67 (2017) 300–308.

[53] D. Bahnemann, R. Dillert, J. Dzengel, R. Goslich, G. Sagave, H-W.Schumacher Field Studies of Solar Water Detoxification Using Non Light Concentrating Reactors, J. Adv. Oxid. Technol. 4 (1999) 11-19.

[54] R. P. Schwarzenbach, P. M. Gschwend, D. M. Imboden, Environmental Organic Chemistry, Wiley-Interscience, New Jersey, 2003.

[55] G. Li Puma, P.L. Yue, P.L., Modelling and Design of Thin-Film Slurry Photocatalytic Reactors for Water Purification, Chem. Eng. Sci. 58 (2003) 2269-2281.

[56] B. Plavac, I. Grčić, I. Brnardić, V. Grozdanić, S. Papić, Kinetic Study of Salicylic Acid Photocatalytic Degradation Using Sol–Gel Anatase Thin Film with Enhanced Long-Term Activity, Reac. Kinet. Mech. Cat. 120 (2017) 385–401.

[57] B. Toepfer, A. Gora, G. Li Puma, Photocatalytic Oxidation of Multicomponent Solutions of Herbicides: Reaction Kinetics analysis with Explicit Photon Absorption Effects, Appl. Catal. B 68 (2006) 171−180.

[58] I. Grčić, G. Li Puma, Photocatalytic Degradation of Water Contaminants in Multiple Photoreactors and Evaluation of Reaction Kinetic Constants Independent of Photon Absorption, Irradiance, Reactor Geometry, and Hydrodynamics, Environ. Sci. Technol. 47 (2013) 13702−13711.

[59] S.Yurdakal, V. Loddo, B. Bayarri Ferrer, G. Palmisano, V. Augugliaro, J. Giménez Farreras, L. Palmisano, Optical Properties of TiO_2 Suspensions: Influence of pH and Powder Concentration on Mean Particle Size, Ind. Eng. Chem. Res. 46 (2007) 7620-7626.

[60] N.A. Kouamé, O.Tahiri Alaoui, A. Herissan, E. Larios, M. José-Yacaman, A. Etcheberry, C. Colbeau-Justin, H. Remita, Visible Light-Induced Photocatalytic Activity of Modified titanium(IV) Oxide with Zero-Valent Bismuth Clusters, New J.Chem. 39 (2015) 2316-2322.

[61] Y.Xu,. H. Lin, L. Li, X. Huang, G. Li, Precursor-Directed Synthesis of Well-Faceted Brookite TiO_2 Single Crystals for Efficient Photocatalytic Performances, J. Mater. Chem. A 3 (2015) 22361-22368.

[62] R. Praveen, R. Ramaraj, Reduced Graphene Oxide-P25-Au Nanocomposite Materials and their Photoelectrocatalytic and Photocatalytic Applications, Photochem. Photobiol. Sci. 15 (2016) 1310-1317.

[63] T. Ohsada, F. Izumi, Y. Fyiki, Raman Spectrum of Anatase, TiO_2, J. Raman Spec. 7 (1978) 321-324.

[64] Q. Kang, J. CaO, Y.Zhang, L. Liu, H. Xu, Y. Ye, Reduced TiO_2 nanotube Arrays for Photoelectrochemical Water Splitting, J. Mater. Chem. A 1 (2013) 5766-5774.

[65] M. Yu, Y. Chen, C. Li, S. Yan, H. Cui, X. Zhu, J. Kong, Studies of oxide growth location on anodization of Al and Ti provide evidence against the field-assisted dissolution and field-assisted ejection theories, Electrochemistry Communications 87 (2018) 76-80.

[66] M. Yu, C. Li, Y. Yang, S. Xu, K. Zhang, H. Cui, X. Zhu, Cavities between the double walls of nanotubes: Evidence of oxygen evolution beneath an anion-contaminated layer, Electrochemistry Communications 90 (2018) 34-38.

[67] G. Bertoni, E. Beyers, J. Verbeeck, M. Mertens, P. Cook, E. F. Vansant, G. Van Tendello, Quantification of Crystalline and Amorphous Content in Porous TiO_2 Samples from Electron Energy Loss Spectroscopy, Ultramicroscopy 106 (2006) 630-635.

[68] S. Tominaka, H. Yoshikawa, Y. Matsushita, A. K. Cheetham, Reduction of Oxide Nanomaterials: Unique Structure and Electronic Properties of Reduced TiO_2 Nanoparticles, Mater. Horiz. 1 (2014) 106-110.

[69] Y. Xu, C. Zhang, L. Zhang, X. Zhang, H. Yao, J. Shi, Pd-Catalyzed Instant Hydrogenation of TiO_2 with Enhanced Photocatalytic Performance, Energy Environ. Sci. 9 (2016) 2410-2417.

[70] W. Hou and S. B. Cronin, A Review of Surface Plasmon Resonance-Enhanced Photocatalysis, Adv. Funct. Mat. 23 (2013) 1612-1619.

[71] F. Le, D. W. Brandl, Y. A. Urzhumov, H. Wang, J. Kundu, N. J. Halas, J. Aizpurua, P. Nordlander, Nanoparticle Arrays: a Common Substrate for both Surface-Enhanced Raman Scattering and Surface-Enhanced Infrared Absorption, ACS Nano 2 (2008) 707–718.

[72] S. L. Zou, G. C. Schatz, Silver Nanoparticle Array Structures that Produce Giant Enhancements in Electromagnetic Fields, Chem. Phys. Lett. 403 (2005) 62–67.

[73] V. Mizeikis, E. Kowalska, S. Juodkazis, Resonant Localization, Enhancement, and Polarization of Optical Fields in Nano-Scale Interface Regions for Photo-Catalytic Applications, J. Nanosci. Nanotechnol. 11 (2011), 2814–2822.

[74] Z. Li, F. Wang, A. Kvit, X. Wang, Nitrogen Doped 3D Titanium Dioxide Nanorods Architecture with Significantly Enhanced Visible Light Photoactivity, J. Phys. Chem. C 119 (2015), 4397-4405.

[75] Q. Li, J. K. Shang, Self-Organized Nitrogen and Fluorine Co-doped Titanium Oxide Nanotube Arrays with Enhanced Visible Light Photocatalytic Performance, Environ. Sci. Technol. 43 (2009), 8923–8929.

[76] D.J. Bertino, R.G. Zepp, . Effects of Solar Radiation on Manganese Oxide Reactions with Selected Organic Compounds, Environ. Sci. Technol. 25 (1991) 1267-73.

Figure captions:

Figure 1. Raman spectra of: a) TiO_2 NT's, b) TiO_2 NT's@Ag, c) TiO_2 NT's@Ag-HA

Figure 2. Scanning electron microscopy images with different magnification: a), b) and c) TiO_2 NT'@Ag and d), e) and f) of TiO_2 NT'@Ag-HA

Figure 3. HAADF STEM images of cross-section TiO_2 NT's@Ag sample: a) smaller magnification and b) higher magnification, c) and d) HRTEM micrographs of TiO_2 NT's@Ag with denoted crystal lattice distances, e) HRTEM micrograph of embedded Ag nanoparticles into TiO_2 nanotubes surface, f) Size distribution of silver nanoparticles

Figure 4. HRTEM of nanotube outer walls on both sides a) and b) of sample TiO_2 NT'@Ag-HA. The amorphous layers are separated by the line.

Figure 5. EELS spectra of bulk and surface: a) core-loss Ti-L2,3 and b) O-k edge of TiO2 NT's-HA, c) core-loss Ti-L2,3 and d) O-k edges of TiO2 NT's@Ag-HA. Insets in Figure a) and c) show STEM-HAADF images with squares which represent area at the nanotube wall where spectra were acquired.

Figure 6. EELS obtained at nanotubes walls of TiO2 NT's, TiO2 NT's-HA and TiO2 NT's@Ag-HA: a) core-loss Ti-L2,3 and b) O-k edges. STEM-HAADF images and squares in represent area of the nanotube walls where EELS maps were acquired. Each spectrum represents sum of EELS map 20x20 pixels.

Figure 7. UV-Visibe spectroscopy results: a) Diffuse reflectance (% R) spectra of pristine TiO_2 NT's, and TiO_2 NT's@Ag before and after reduction treatment, b) Kubelka-Munk absorption curves. c) Determination of band gap of each samples by drawing a line at $[F(R)*h\upsilon]^{1/2}=0$. Inset in the Fig. 8c represent magnified curve of The sample TiO2 NT's-HA in energy range 1.5-2 eV.

Figure 8. Schematic view of Ag local plasmon resonance effect and band position at the interface of Ag and TiO_2.

Figure 9: Kinetics of photolysis and photocatalytic degradation of SA: a) under full-spectrum solar irradiation and b) visible irradiation (photolysis was negligible), using TiO_2 NT's, TiO_2 NT's@Ag and TiO_2 NT's@Ag-HA as photocatalysts ($C_{0,SA}$ = 0.2 mmol dm^{-3}, pH 4) .

Figure 10. Results of photocatalytic tests: a) Comparison of mineralization and aromatic cleavage efficiencies achieved by photocatalysis under simulated solar and visible irradiation using Ag-doped TiNTs (irradiation time was 120 min); b) Stability of the photocatalytic films under full-spectrum solar irradiation expressed as the observed reaction rate constant per cycle.

Figure 11. Kinetics of photocatalytic degradation of SA under full-spectrum solar irradiation and visible irradiation using TiO_2 NT's@Ag and TiO_2 NT's@Ag-HA as photocatalysts ($C_{0,\,SA}$ = 0.2 mmol dm^{-3}, pH 4); experimental results *vs.* model.

Graphical Abstract (for review)

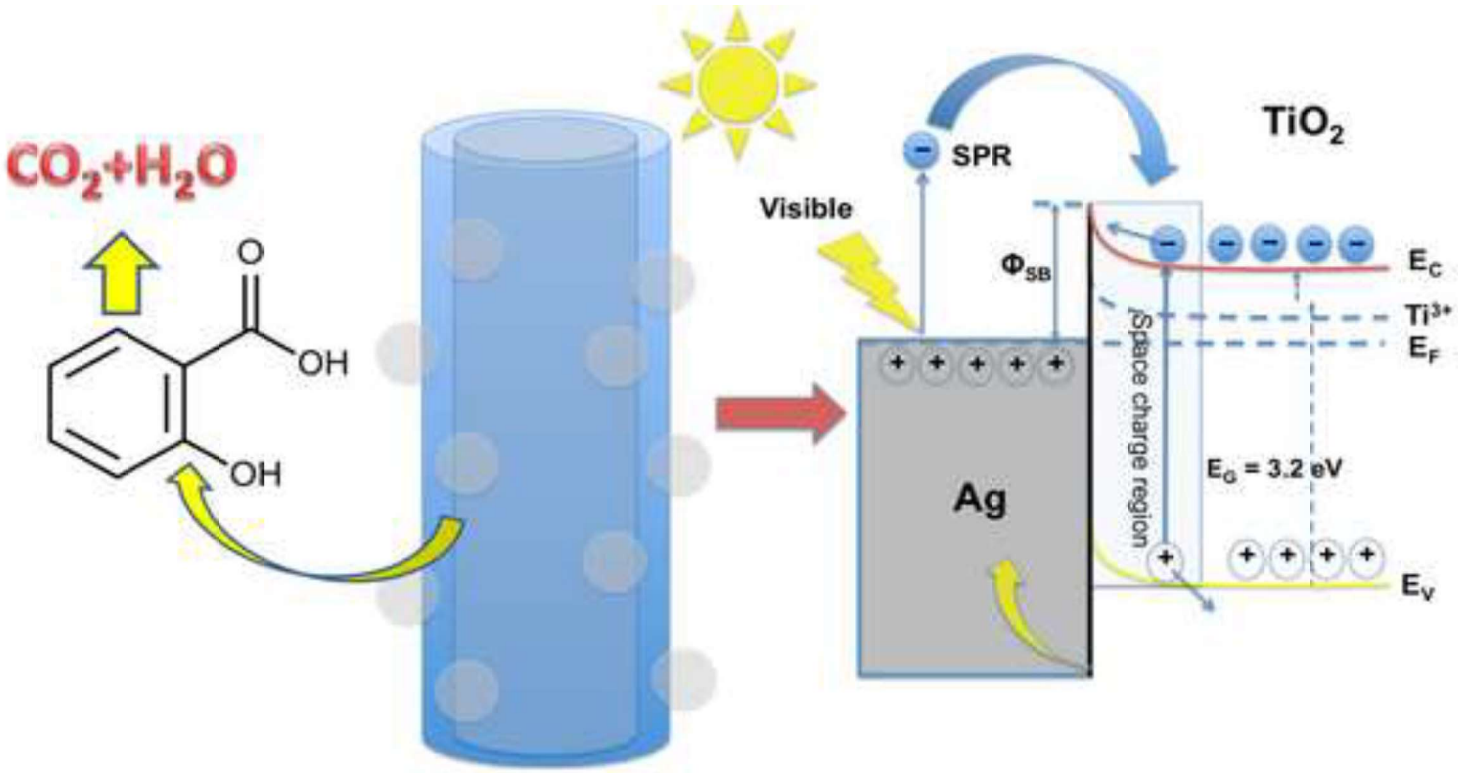

Highlights:

- Black TiO_2 with Ag nanoparticles for photocatalytic degradation of salicylic acid.
- Better than P25 due to combined effect of Ti^{3+} and local surface plasmon resonance.
- Completely attached to the surface - easy handling and removal from purified water.
- Enhancement in the photocatalytic efficiency under visible light irradiation.
- Complex kinetic model of catalysis for quantification of different effects.

Tables

Table 1. The pseudo-first order rate constant ($k_{SA,\ obs}$) for the degradation of SA in the flow cell using TiO_2 NT's, TiO_2 NT's@Ag, TiO_2 NT's@Ag-HA as photocatalysts irradiated with simulated solar and visible irradiation.

sample	Full-spectrum solar irradiation			Visible irradiation		
	$k_{SA,obs} \times 10^3$, min^{-1}	$t_{1/2}$, h	R^2	$k^{vis}_{SA,obs} \times 10^3$, min^{-1}	$t_{1/2}$, h	R^2
TiO_2 NT's	2.19 ± 0.07	4.6	0.9718	0.09	125.2	0.9655
TiO_2 NT's @Ag	2.98 ± 0.14	3.7	0.9966	0.56	20.0	0.8269
TiO_2 NT's Ag-HA	5.81 ± 0.13	1.9	0.9966	1.29	8.5	0.9371
photolysis	$k_{p,\ obs} = (1.99 \pm 0.06) \times 10^{-3}$ min^{-1}			$k_{p,\ obs} \approx 0$		

Table 2. Intrinsic reaction rate constant, absorption terms and factors of synergy for the degradation of SA in the flow cell over TiO_2 NT's, TiO_2 NT's@Ag, TiO_2 NT's@Ag-HA irradiated with simulated solar irradiation.

term	TiO_2 NT's	TiO_2 NT's@Ag	TiO_2 NT's@Ag-HA
$k_{SA,\,int}$, $s^{-1}\,W^{-0.5}\,m$	1.4×10^{-8}		
$\kappa^*_{P25,\,310\,nm}$, $m^2\,kg^{-1}$	508 [58]		
$\kappa^*_{P25,\,365\,nm}$, $m^2\,kg^{-1}$	187 [56,57]		
$\mu'_{app,310nm}$	1050	91 000	15 000 000
$\mu'_{app,365nm}$	1350	130 000	20 500 000
$\mu''_{app,310nm}$	1	1.24	1.47
$\mu''_{app,365nm}$	1	1.29	1.53
P_{ph}^{vis}, $10^5\,W\,m^{-2}$	0.12	4.71	25.94
f_{Syn}	(1.08 ± 0.05)*	1.36 ± 0.25	± 0.14

* Error was determined based on experimentally determined $k_{SA,\,obs}$ in experiments with different $C_{SA,0}$

Figure 1
Click here to download high resolution image

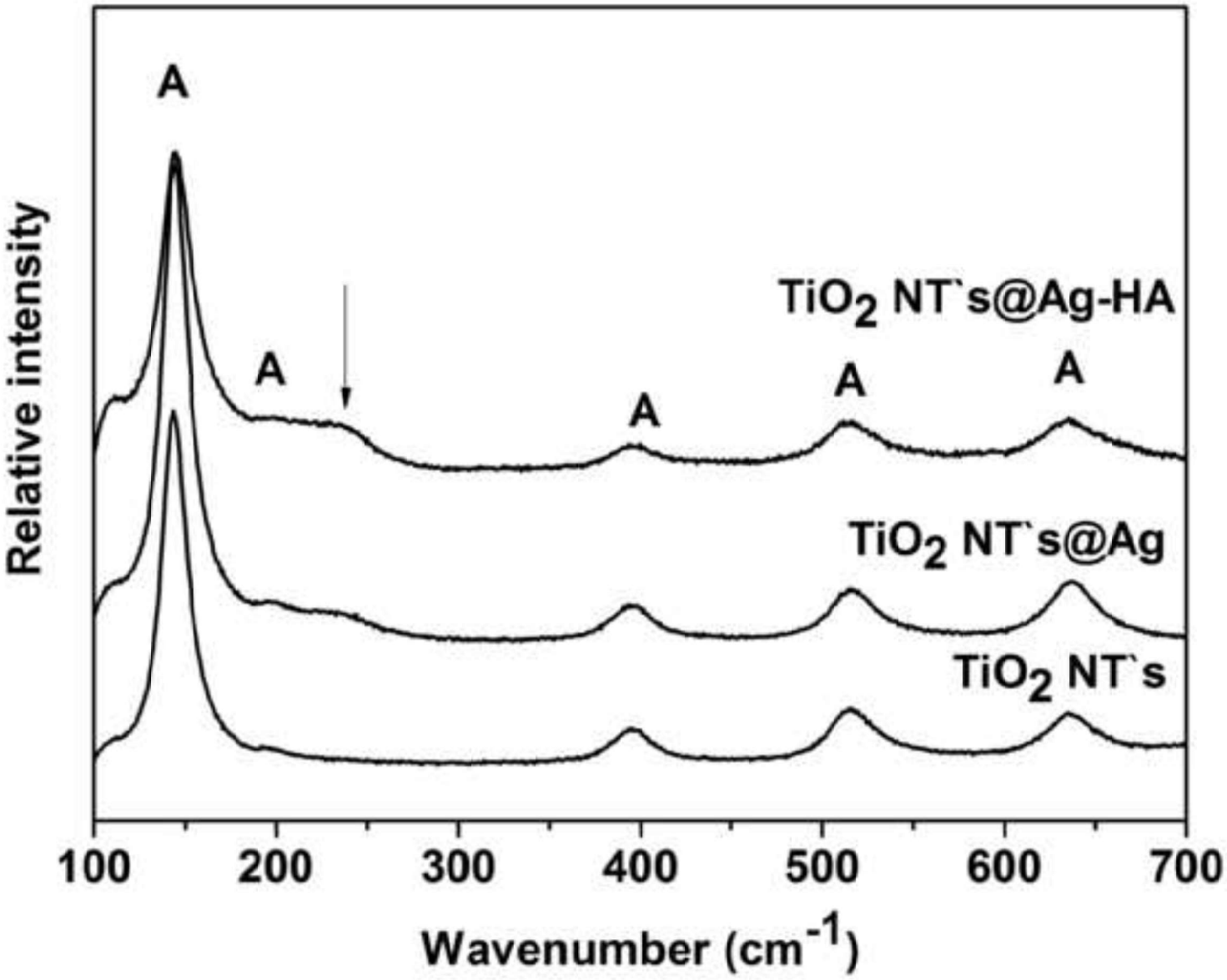

Figure 2
Click here to download high resolution image

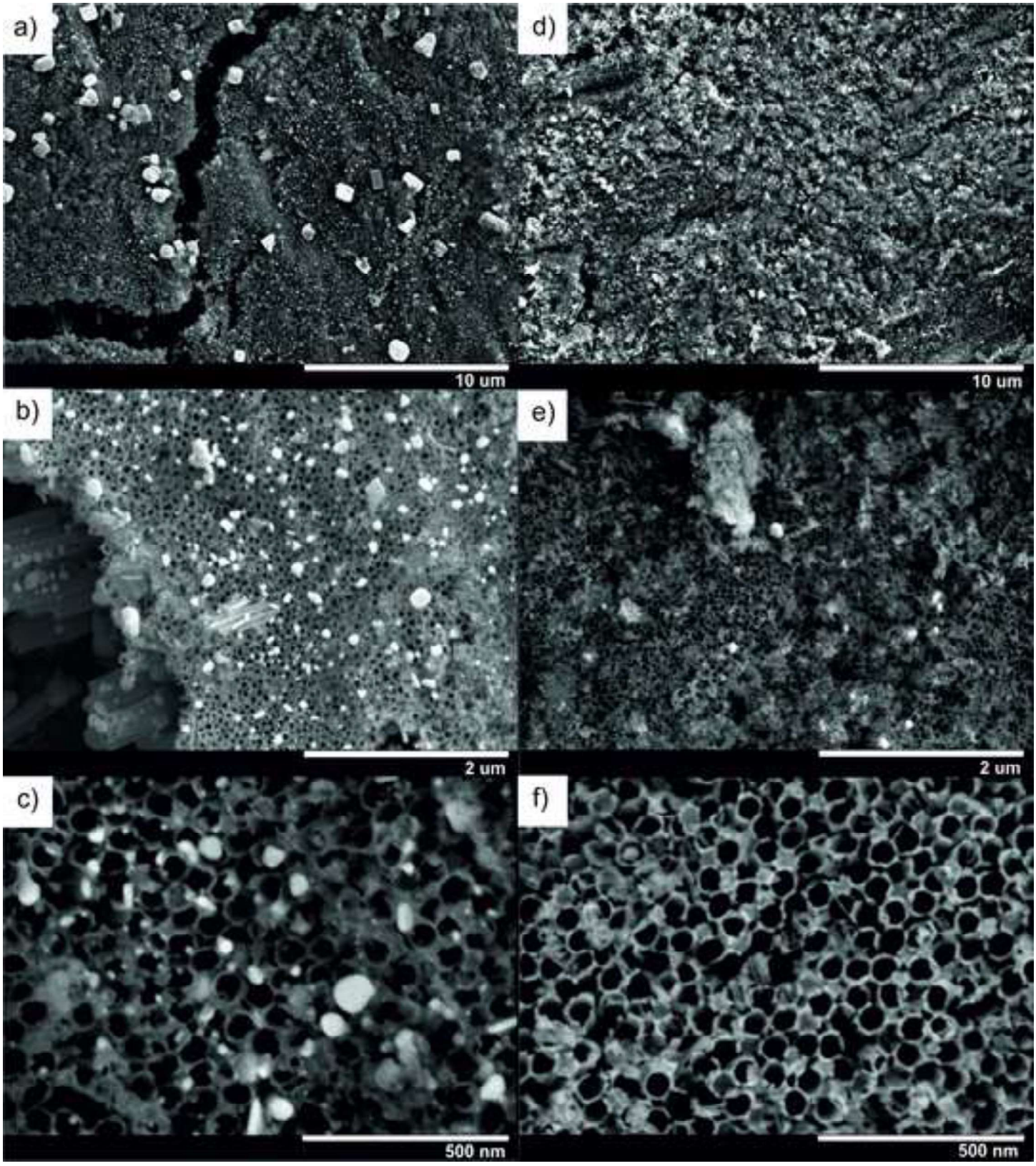

Figure 3
Click here to download high resolution image

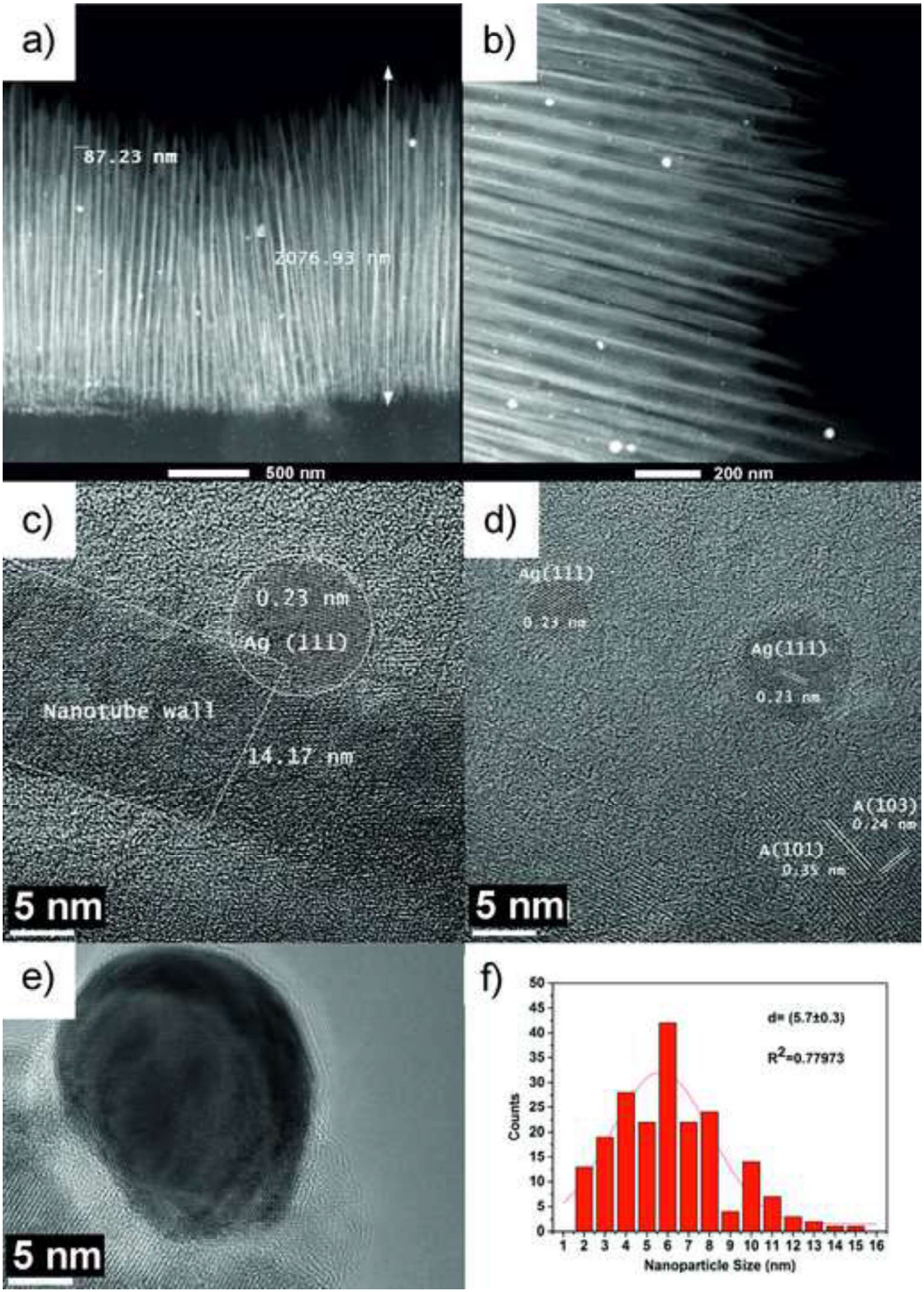

Figure 5

Click here to download high resolution image

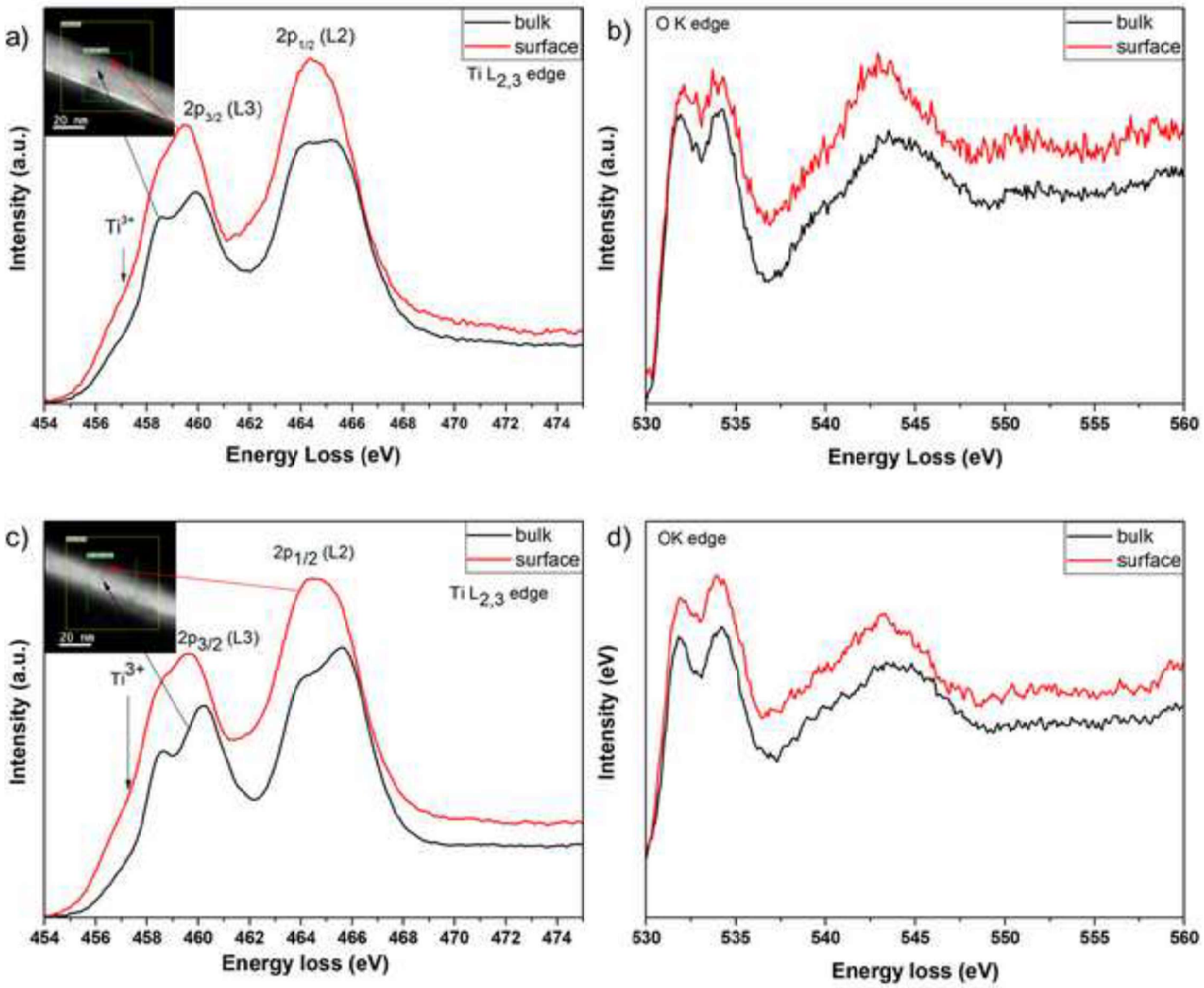

Figure 6

Click here to download high resolution image

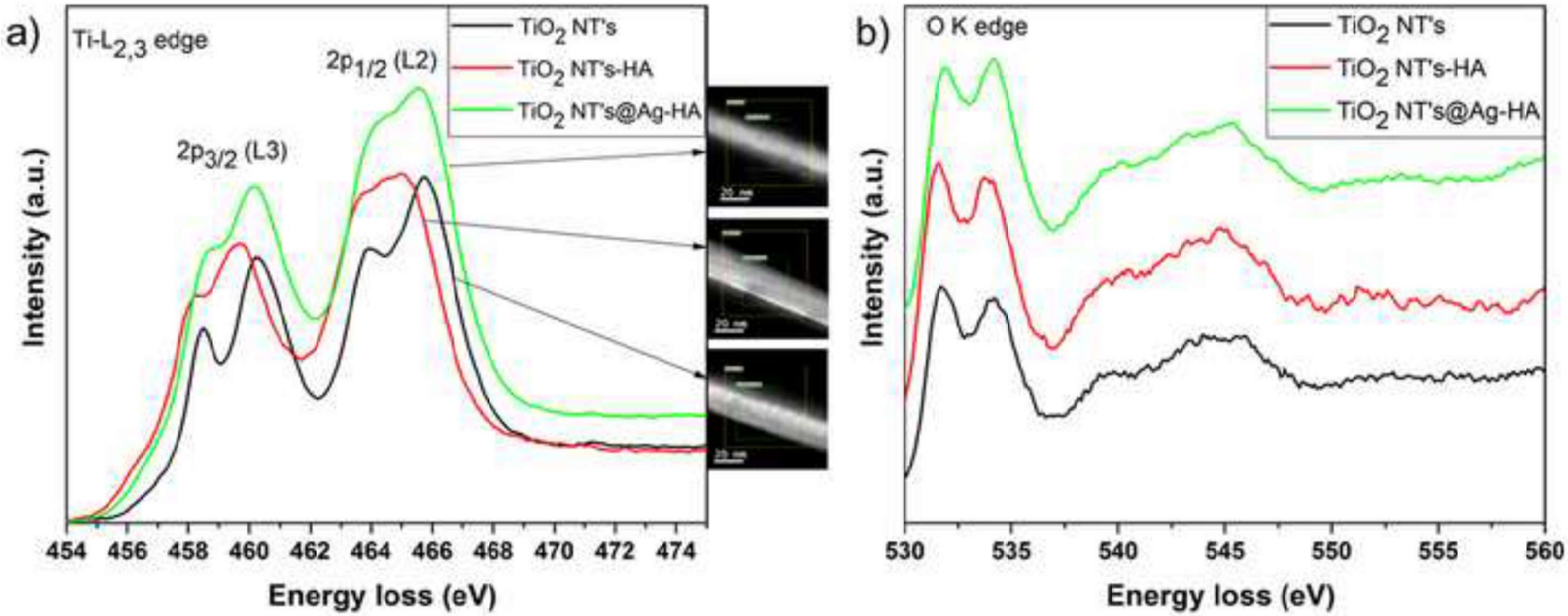

Figure 7
Click here to download high resolution image

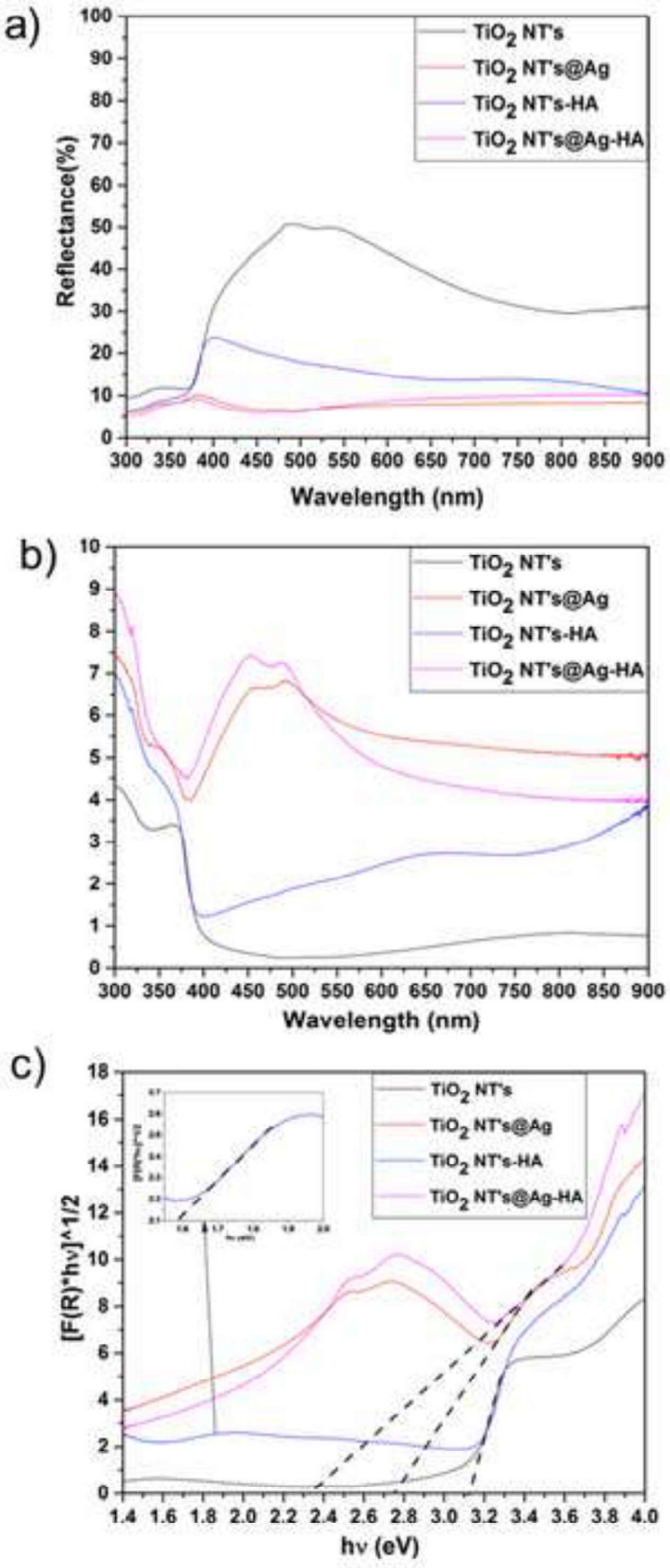

Figure 8

Click here to download high resolution image

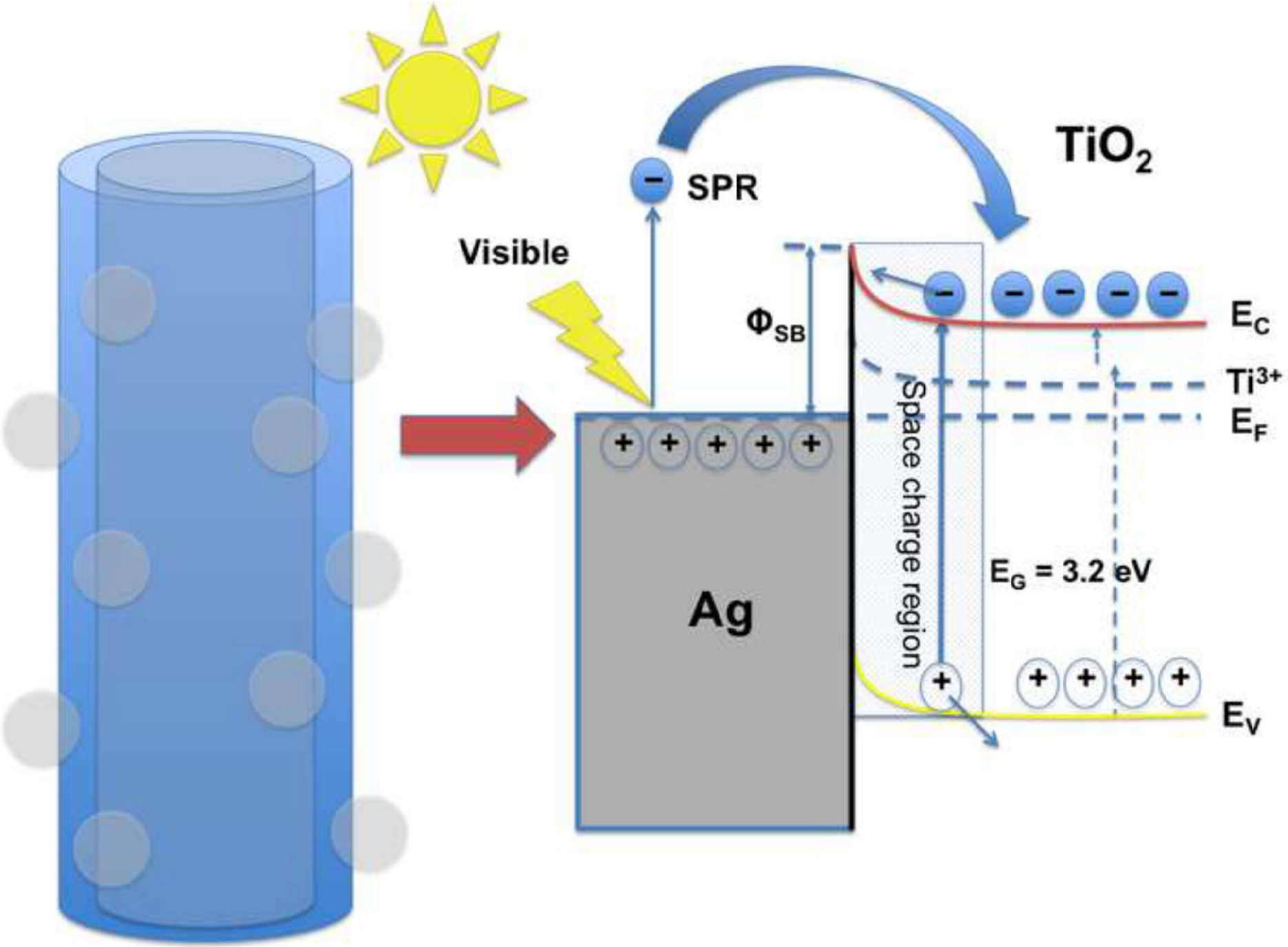

Figure 9

Click here to download high resolution image

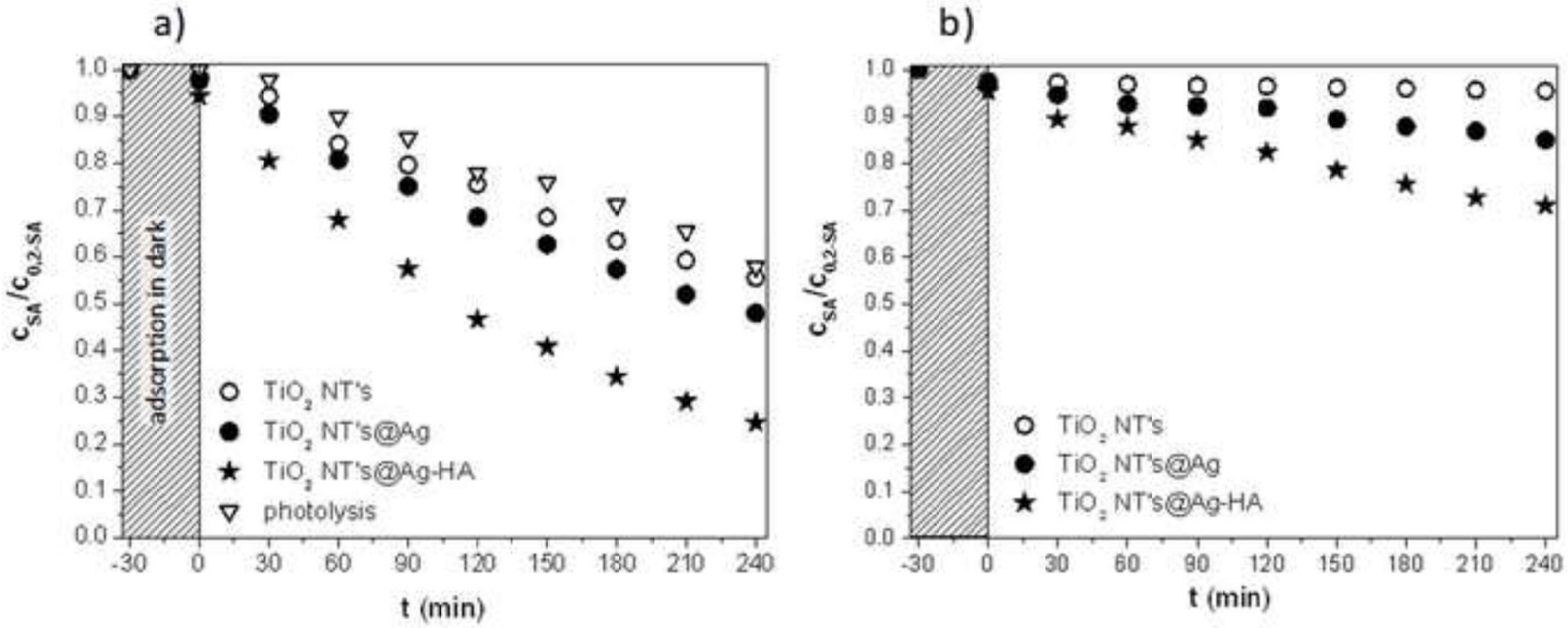

Figure 11

Click here to download high resolution image

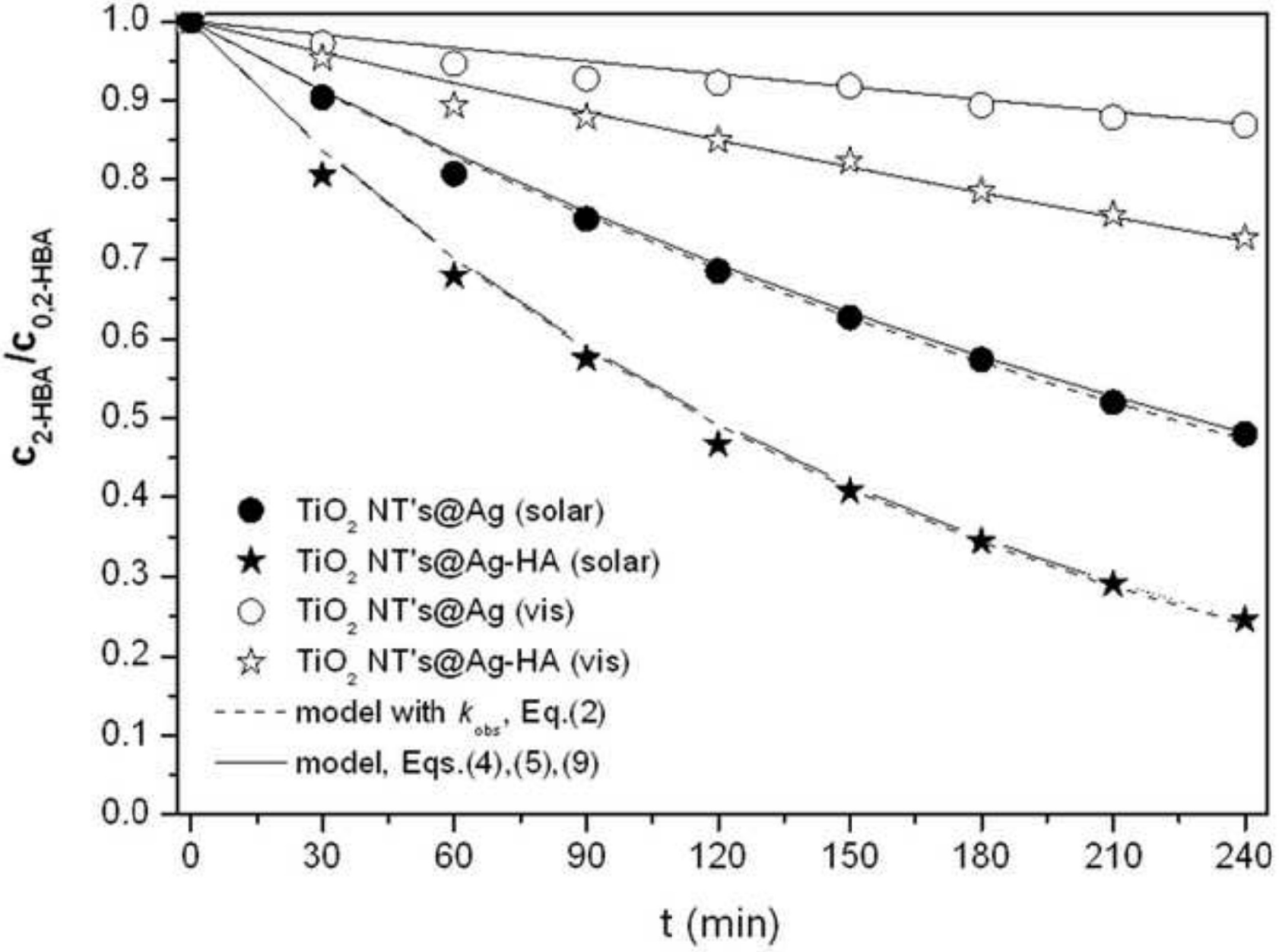

Figure 4_new
Click here to download high resolution image

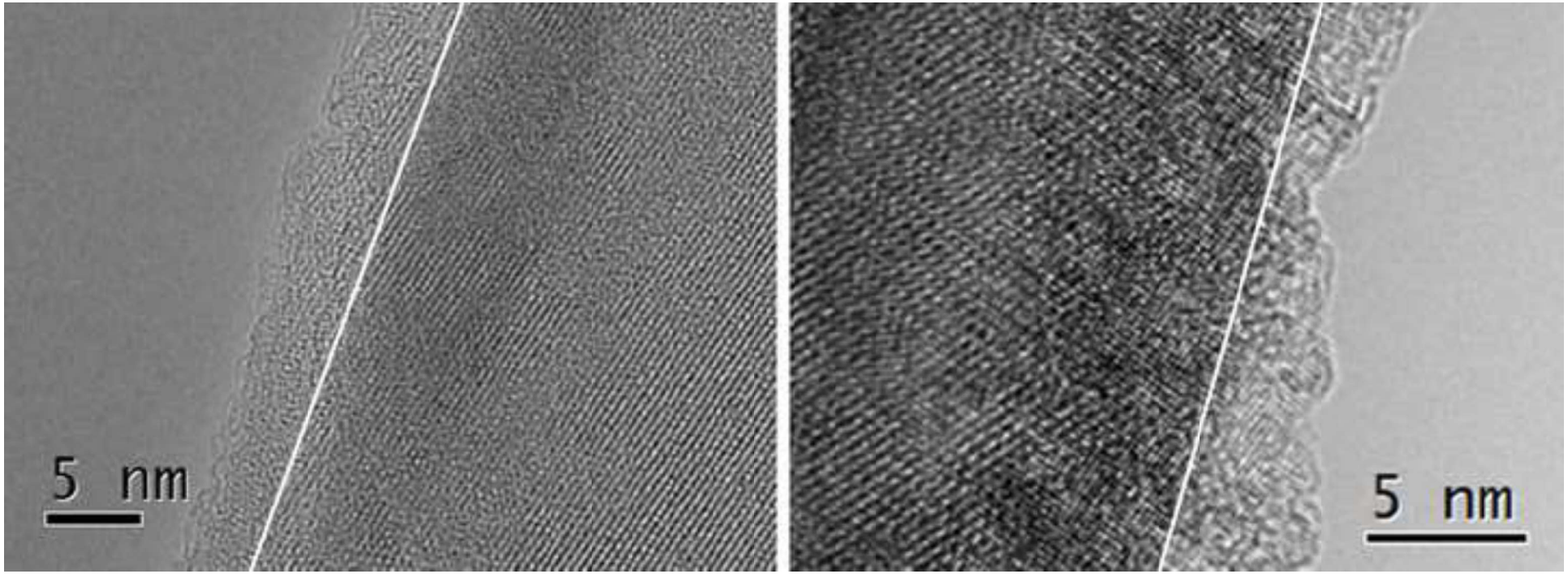

Figure 10_new
Click here to download high resolution image